RESEARCH ARTICLE | FEBRUARY 09 2026

Bubble dynamics in a pore-doublet system under vibration

Wen Deng (邓文) ; Shilin Yu (于仕霖) ; Wenbao Zheng (郑文葆); Chao Zeng (曾超) ; Chaozhong Qin (秦朝中)

Physics of Fluids 38, 023314 (2026)
https://doi.org/10.1063/5.0312708

Physics of Fluids ARTICLE pubs.aip.org/aip/pof

Bubble dynamics in a pore-doublet system under vibration

Cite as: Phys. Fluids **38**, 023314 (2026); doi: 10.1063/5.0312708
Submitted: 18 November 2025 · Accepted: 21 January 2026 ·
Published Online: 9 February 2026

View Online Export Citation CrossMark

Wen Deng (邓文),[1,a)] Shilin Yu (于仕霖),[1] Wenbao Zheng (郑文葆),[1] Chao Zeng (曾超),[2] and Chaozhong Qin (秦朝中)[3,a)]

AFFILIATIONS

[1]School of Civil Engineering, Southeast University, Southeast University Road, Jiangning District, Nanjing, China
[2]Physical and Computational Science Directorate, Pacific Northwest National Laboratory, Richland, Washington 99352, USA
[3]School of Resources and Safety Engineering, Chongqing University, Chongqing, China

[a)]**Authors to whom correspondence should be addressed:** wendeng@seu.edu.cn and chaozhong.qin@gmail.com

ABSTRACT

The dynamics of trapped gas bubbles in porous media under vibrational excitation are crucial for understanding multiphase transport behavior. While conventional single-channel models often neglect the presence of bypass wetting flow, such flow paths can significantly influence bubble resonance and mobilization thresholds. In this study, we develop a pore-doublet model that explicitly captures the interaction between a trapped non-wetting bubble and the bypassing wetting phase within a two-channel pore geometry. By integrating capillary, viscous, and inertial forces, the model reveals how bypass wetting flow affects the oscillatory behavior of the bubble under harmonic vibration. Analytical and numerical analyses in both the frequency and time domains show distinct differences between pore-doublet and single-channel models, particularly in terms of resonance frequency shifts and amplitude responses related to effective permeability. The model is further validated against computational fluid dynamics simulations. These results provide new insights into bubble–fluid interactions in vibrated porous systems and offer a framework for modeling multiphase flow under dynamic excitation.

NOMENCLATURE

$a(t)$, A	Excited acceleration, amplitude of acceleration
a_ρ, a_μ	Density ratio, viscosity ratio (wetting to nonwetting)
A_c	Amplitude of particular acceleration by a seismic wave at which the trapped bubble becomes freed
A_u, A_d	Cross-sectional areas of the tube at the contact line of the rear and front menisci
$\cos\theta/R$	Curvature of the wetting/nonwetting interface
F_x, F_p, F_a	Viscous force, pressure force along the wall, oscillatory force
h, s_0	Transient positions of the three-phase contact line
k	Permeability of surrounding pores
L	Spatial semi-wavelength of the constriction
L_0	Length of straight tube
L_u, L_d	Axial coordinates at the entrance and exit of the model geometry
m, b, k_0, F	Mass, damping coefficient, coefficient of recovering force, and amplitude of harmonic loading in a linear oscillator
$M1(x)$, $M2(x)$, $M3(x)$, $M4(x)$	Introduced functions of position x
M_{eff}	Effective mass
$N1(x)$, $N2(x)$, $N3(x)$, $N4(x)$	Introduced functions of position x
Oh	Ohnesorge number
P_{cu}, P_{cd}	Capillary pressure at the rear and front menisci
P_g, V_g	Gas pressure and bubble volume
P_g^i, V_g^i	Gas pressure and bubble volume at the initial stationary state
P_u, P_d	Entrance and exit background pressure
P_u, P_d	Pressure of wetting liquid at the rear and front menisci
Q, Q_1, Q_2	Flow rate in the inlet, straight tube, and constricted tube, respectively
r	Radius of a straight tube
r_0, f_0	Peak of amplitude ratio, associated resonance frequency
r_{max}, r_{min}	Maximum and minimum radii of the tube
β, x^*	Defined dimensionless variables
ΔP_c	Capillary resistance

ΔP_e	External pressure difference
θ	Contact angle
Λ	Aspect ratio of constriction
λ(x)	Tube radius at axial position x
λ_{men}(s) λ_{men}(h)	Radius of curvature for the rear and front menisci
μ_w, μ_n	Density of wetting/nonwetting phase
ξ	Amplitude ratio
ρ_w, ρ_n,	Dynamic viscosity of wetting/nonwetting phase
σ	Interfacial tension of the wetting/nonwetting interface
τ	Time scale for the Hagen–Poiseuille starting flow to fully develop
X_0	Dimensionless natural frequency
X_n	Dimensionless excitation frequency
$\chi(\omega)$	Frequency response function
ω, f	Angular frequency and frequency of excitation
ω_c^n	Characteristic frequency of the nonwetting phase

I. INTRODUCTION

Subsurface formations typically consist of a solid skeleton, pore water, and entrapped gas bubbles, forming a representative multiphase and multiscale heterogeneous system. The presence of gas bubbles significantly alters the hydrological properties, mechanical responses, and acoustic behaviors of porous media, and is ubiquitous in both natural and engineered environments. Such bubbles may originate from natural processes such as microbial gas production,[1] hydrocarbon degradation,[2] groundwater level fluctuations,[3] or changes in gas solubility, as well as from anthropogenic activities including air injection,[4] foam flooding,[5] heavy oil viscosity reduction,[6] gas hydrate exploitation,[7] and CO_2 geological sequestration.[8] Under buoyant forces, bubbles tend to ascend. However, during their motion, they may grow, coalesce, or become immobilized at pore throats due to convergent–divergent geometries, known as the Jamin effect,[9,10] which reduces fluid connectivity and lowers effective permeability.

When subjected to external vibration excitation, such as seismic or acoustic waves, these trapped bubbles may oscillate and undergo microscale migration, dynamically modulating the permeability, damping characteristics, and effective elastic modulus of the porous medium.[11–13] At the macroscopic level, such nonlinear microscale responses can manifest as vibration-induced phenomena, including sudden changes in groundwater levels, mud volcano eruptions, debris flows, and even soil liquefaction.[14] Despite their broad implications, the nonlinear mechanisms underlying bubble oscillation and mobilization under vibrational forcing remain inadequately understood. This knowledge gap arises from two main challenges. First, these processes occur at micrometer to millimeter scales and involve strong nonlinearities, making direct observation difficult.[15] Second, when the excitation frequency approaches the bubble's natural resonance frequency, energy dissipation and nonlinear fluid–structure interactions become significant, complicating theoretical modeling.[16,17] Therefore, predictive models are needed to characterize the nonlinear oscillation behavior of trapped bubbles under vibrational forcing, and to capture their resonance response across varying permeability and excitation conditions.

Despite recent efforts, few microscale models describe nonwetting phase dynamics in pores, typically for liquid droplets. These models are primarily based on force balance,[18] pressure balance,[19,20] or momentum balance.[21] To systematically delineate the scope of these established frameworks and highlight the specific gaps addressed in this study, we summarize their respective contributions and limitations in Table I. However, these models commonly adopt simplified single-channel representations with fixed pressure boundary conditions. In real porous systems, residual bubbles are surrounded by bypassing wetting fluids, creating local pressure fluctuations that challenge the validity of fixed-pressure assumptions. Furthermore, conventional models often overlook how adjacent pore permeability influences system dynamics, limiting their accuracy in predicting bubble entrapment, resonance, and release. While experimental and numerical investigations have explored residual droplet dynamics under vibration,[22–25] they typically adopt simplified straight-channel geometries that neglect the geometry-induced capillary resistance critical in realistic pore-throat structures. To address these limitations, some studies have introduced the pore-doublet model to better capture the coupled dynamics of two-phase flows.[26,27] However, these models are often conceptual and lack the dynamic predictive capability needed for vibration-driven systems.

Building on the momentum balance approach by Deng and Cardenas,[21] we formulate a pore-doublet model that, for the first time, explicitly accounts for bypassing wetting flow in bubble oscillation dynamics under vibration. While three-dimensional studies have highlighted the complexity of the non-wetting/wetting interface during bubble oscillations,[28–30] we employ a one-dimensional spherically shaped meniscus approximation as a physically consistent and analytically tractable simplification.[19,21] This approach captures the essential coupling among capillary, inertial, and viscous forces while maintaining model feasibility.

Using this model, we comprehensively characterize bypass-modulated bubble dynamics under vibrational forcing. We evaluate modeling assumptions and predictive performance in the frequency domain, while examining resonance responses under varying amplitudes in the time domain. As the forcing amplitude increases, we investigate the required threshold for bubble mobilization and validate model predictions against computational fluid dynamics (CFD) simulations. We further quantify how heterogeneities in the permeability of adjacent pores modulate the nonlinear resonance characteristics of trapped bubbles. Collectively, this analysis establishes a rigorous theoretical framework for bypass-driven nonlinear bubble behavior under vibration and provides physical insights into energy dissipation and frequency-dependent flow modulation in porous media.

II. THEORETICAL MODEL OF THE BUBBLE

A. Problem statement

In porous media, bubble migration is governed by the coupled effects of capillary forces, inertia, buoyancy, gravity, and external perturbations,[31–33] with the overall behavior strongly influenced by the spatial inclination of the pore channels.[34,35] To facilitate theoretical analysis, we focus on bubble dynamics in horizontally aligned channels, where the combined effects of buoyancy and gravity are treated as an equivalent, steady background pressure gradient. This simplification allows us to neglect buoyancy-induced disturbances and isolate the influence of vibrational forcing on bubble motion, particularly in terms of how vibration excitation governs bubble unlocking and nonlinear migration.

TABLE I. Comparison of theoretical models.

Model type	Representative studies	Bypass flow treatment	Inertial effects handling	Key limitations (addressed by current work)
Pressure-balance model	Hilpert *et al.*[20]	Ignored	Captures inertial effects	Fails to account for bypass flow effects and viscosity dissipation during mobilization.
Force-balance model	Beresnev[18]	Ignored	Assumes fixed external pressure gradient	Neglects the impact of bypass flow and pressure redistribution on bubble dynamics.
Single-channel momentum model	Deng and Cardenas[21]	Ignored	Captures internal fluid inertia	Captures internal fluid inertia, but fails to account for bypass-induced "added mass" and "flow damping."

Extensive studies have shown that bubble entrapment primarily arises from capillary pressure imbalances induced by pore geometry. According to the Young–Laplace equation, capillary pressure is governed by interfacial tension and contact angle. In convergent–divergent pore throat geometries, a pressure difference arises between the upstream and downstream menisci, giving rise to a geometric capillary resistance. Unlike the intrinsic capillary pressure across the two-phase interface, this resistance originates from the curvature differences imposed by pore-throat convergence and divergence. Under natural reservoir pressure gradients or engineered driving forces, such as water flooding or contaminant remediation, bubbles remain immobilized when the external pressure gradient is insufficient to overcome this capillary resistance. This capillary resistance forms a threshold condition for bubble mobilization, which is incorporated into our theoretical model through the pressure balance at the menisci.

This capillary resistance creates a threshold condition that must be overcome for bubble displacement to occur. The critical pressure gradient, the minimum pressure gradient required to displace a trapped bubble, is primarily controlled by capillary resistance and is largely insensitive to viscous shear. When the applied pressure gradient is below this critical value, bubble migration through the pore throat is extremely slow, and viscous shear stresses are negligible. Once the threshold is exceeded, however, the bubble can be released even under low flow velocities.

Under vibration excitation, the porous medium is subjected to periodic oscillatory forces that act as time-dependent perturbations superimposed on the background pressure gradient. These transient oscillations can intermittently overcome local capillary resistance, thereby inducing bubble oscillation and potential displacement. Unlike steady pressure-driven flow, vibrational forcing introduces rapid fluctuations in both amplitude and direction, leading to strongly nonlinear system responses. In such regimes, viscous dissipation becomes the dominant energy loss mechanism.

Additionally, thin wetting films may form at the interface between the wetting and non-wetting phases. Depending on the viscosity ratio of the two fluids, these films can exhibit either lubricating or resistive effects. As a result, realistic modeling of bubble dynamics under vibration must account for the viscosities of both phases, interfacial boundary-layer effects, and the frequency-dependent characteristics of the system's dynamic response. These considerations form the basis for the governing equations and boundary conditions presented in Sec. II C.

The central objective of this study is to investigate how the frequency and acceleration amplitude of vibrations influence the oscillatory behavior and mobilization threshold of trapped bubbles. To this point, we have developed a pore-doublet model based on the momentum balance framework proposed by Deng and Cardenas.[21] This model explicitly incorporates bypassing wetting flow effects and captures the key mechanisms underlying bubble dynamics under vibrational forcing.

To bridge the gap between complex porous media and theoretical modeling, we simplify the local pore network shown in Fig. 1(a) into a representative pore-doublet model shown in Fig. 1(b). While Fig. 1(a) depicts the topological complexity of natural porous media, Fig. 1(b) isolates a single bubble-trapping event by "lumping" the surrounding complex flow network into a single equivalent bypass channel characterized by an effective permeability. As shown in Fig. 1(b), a fixed aqueous phase flow rate Q is imposed at the inlet, while the outlet pressure is set to zero. The inlet bifurcates into two channels: a straight tube that serves as the equivalent bypass path, and a sinusoidally shaped convergent–divergent constricted tube, where the bubble is trapped upstream at the throat due to capillary forces. The initial conditions are defined to ensure physical consistency: the bubble is initially immobilized in the constricted tube ($Q_2 = Q$), and consequently, the entire imposed flow passes through the straight tube ($Q_1 = Q$). The pressure differences P_u and P_d at the upstream and downstream junctions correspond to the capillary pressure P_{ca} exerted on the bubble interfaces.

Incorporating vibration excitation into the two-phase flow calculations, we model the relative acceleration between the fluid and solid phases as a body force. Our theoretical model consists of two key components: (1) a momentum balance equation derived from the single-channel model that describes the dynamic response of the bubble, and (2) a velocity profile equation based on the Hagen–Poiseuille law, which models the flow of the water phase and accounts for pressure losses. The relationship between the two channels is governed by the equation $Q = Q_1 + Q_2$.

To reduce computational complexity, the irregular cluster of flow paths surrounding the bubble in real porous media is simplified into a single equivalent bypass channel. This conceptual channel [referred to

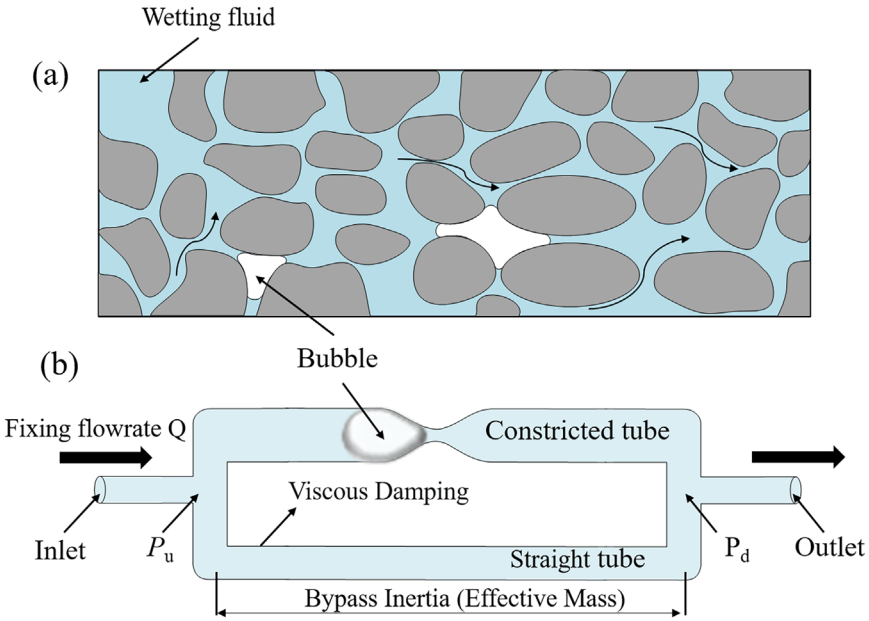

FIG. 1. Schematic representation of porous media and simplified pore-doublet model to analyze bubble passing through a single constriction. The bubble is marked by white in porous media, the wetting fluid is marked by light blue, and the grain is marked by gray color. Annotations in the straight tube indicate that the fluid column contributes to the effective oscillating mass (inertia), while the wall shear stress provides the bypass viscous damping.

as the straight tube in Fig. 1(b)] serves as an effective medium abstraction, aggregating the hydraulic resistance and fluid inertia of the multiple parallel flow paths into a computationally tractable equivalent path. While natural pore networks exhibit tortuosity and geometric complexity, this straight-channel simplification captures the fundamental inertial coupling mechanism, providing a conservative baseline for analyzing bypass-induced resonance shifts. We introduce an effective permeability parameter to approximate the collective hydraulic influence of these bypass routes. This simplification significantly reduces the dimensionality of the parameter space and computational cost, while preserving the key features of system dynamics, thereby enhancing the model's applicability and generalizability.

The model is driven by a single-frequency harmonic input, which allows precise control over the vibration frequency and amplitude and facilitates systematic exploration of how these parameters influence bubble dynamics. Harmonic vibration excitation is also mathematically tractable, enabling analytical and numerical comparisons. This approach aligns with previous studies[19,21] that employed similar forms of excitation, ensuring compatibility and comparability with existing frameworks. By explicitly incorporating bypass effects, contact line motion, and nonlinear oscillatory responses, the proposed model extends the momentum balance framework and offers new theoretical insights into bubble oscillation, unlocking, and release in partially saturated porous media. This enhanced formulation contributes to a more comprehensive understanding of dynamic two-phase interactions under vibration forcing.

B. Pore constriction geometry

We analyzed a model featuring a constricted, axisymmetric tube (see Fig. 2) to represent the flow channel in porous media, a geometry frequently employed in related experimental studies. Cylindrical coordinates (r, x) are employed with the axial origin $(x = 0)$ at the neck of the constriction. The wall surface of a constricted tube follows

$$\lambda(x) = \begin{cases} r_{max}, & L_u < x < -L, \\ \dfrac{r_{max} + r_{min}}{2} - \dfrac{r_{max} - r_{min}}{2} \cos\left(\dfrac{\pi x}{L}\right), & -L \le x \le L, \\ r_{max}, & L < x < L_d, \end{cases} \quad (1)$$

where r_{max} and r_{min} are radii of the pore body and pore throat, respectively. L is the half wavelength of the sinusoidal constriction. L_u and L_d are the coordinates of the entrance and exit of the tube, respectively.

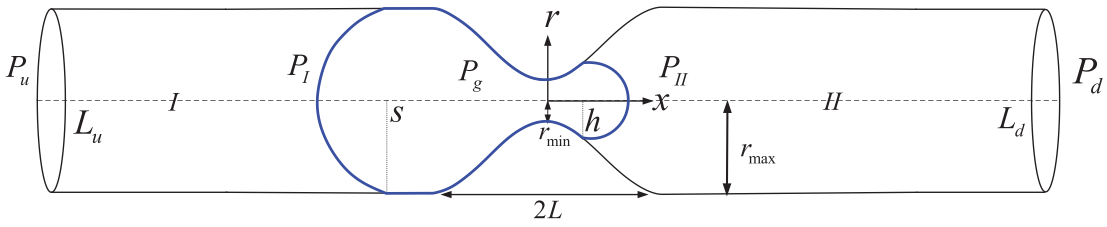

FIG. 2. Gas bubble inside constricted tube 2 just after expansion into the downstream region. The interface of water and bubble is marked by blue color. Model geometric parameters and pressure are labeled as well. The figure annotations and caption have been updated to clarify the axial nature of coordinates s and h. The domain boundaries are now labeled as L_u and L_d.

Momentum balance is applied to the two distinct wetting fluid segments within the constricted tube, designated as fluid domain I and fluid domain II. Fluid domain I represents the upstream liquid slug extending from the inlet ($L_u < x < s$), while fluid domain II represents the downstream liquid slug stretching from the front three-phase contact line to the outlet ($h < x < L_d$). To simplify the analysis, the spherical caps at both the rear and front menisci are included in the control volume of the fluid. This simplification is justified by the significantly greater length of the water plug than that of the spherical caps. In this study, we adopt a one-dimensional framework based on the lubrication approximation and treat the fluid-fluid interfaces as quasi-static hemispherical menisci. While we acknowledge that realistic pore-scale flows exhibit three-dimensional complexities, such as dynamic curvature variations and corner flows, this simplified approach is justified under the low-capillary-number conditions considered here ($Ca < 10^{-4}$). In this regime, surface tension forces significantly dominate over viscous stresses, ensuring that the interface shape is primarily governed by the static Young–Laplace equilibrium. As demonstrated in prior studies, this approximation effectively captures the fundamental displacement dynamics and mobilization thresholds despite the neglect of three-dimensional variations.[21]

C. Momentum balance of upstream fluid in constricted tube

The momentum balance in domain I is first established. The macroscopic governing equation is

$$\rho \frac{d}{dt}\int_V \langle v_x\rangle dV = \rho A_u \langle v_x^2\rangle + P_u A_u - P_I A_I + F_p - F_x + F_a, \quad (2)$$

where the symbol $\langle\cdot\rangle$ implies the average of the quantity over the cross section. The left-hand side is the rate of momentum change in control volume V. On the right-hand side, $\rho A_u \langle v_x^2\rangle$, $P_u A_u$, $P_I A_I$, F_p, F_x, and F_a are momentum influx at inlet, entrance pressure force, exit pressure force, pressure force along the capillary wall, viscous drag, and oscillatory inertial force; ρ is the density of the wetting phase fluid, A_u and A_I are the cross-sectional areas of the inlet of the constricted tube and the three-phase contact positions for the downstream meniscus of wetting fluid, and P_u and P_I are the pressure of the inlet of the constricted tube and three-phase contact positions for the downstream meniscus of wetting fluid.

Let ds/dt be the average flow velocity in domain I, and the flow rate of domain I can be given as

$$Q_1 = \pi\lambda^2(s)\frac{ds}{dt}, \quad (3)$$

where Q_1 is the flow rate of the wetting fluid at the upstream meniscus.

The average velocity can be expressed as

$$\langle v_x\rangle = \frac{\lambda^2(s)}{\lambda^2(x)}\frac{ds}{dt}. \quad (4)$$

The rate of momentum change becomes

$$\rho \frac{d}{dt}\int_V \langle v_x\rangle dV = \pi\rho\lambda^2(s)\left[\left(\frac{ds}{dt}\right)^2 - (s-L_u)\frac{d^2s}{dt^2}\right]. \quad (5)$$

The momentum influx can be calculated from Eq. (2) at x = L_u, where the radius of the tube is r_{max}. Therefore, the momentum influx is

$$\rho A_u \langle v_x\rangle^2 = \frac{4}{3}\pi\rho\frac{\lambda^4(s)}{\lambda^2(x)}\left(\frac{ds}{dt}\right)^2, \quad (6)$$

where the velocity at the entrance is assumed to have a parabolic profile. The factor 4/3 is used to compensate for the average squared velocity in Eq. (4).

The entrance pressure force is

$$P_u A_u = \pi\lambda^2(L_u)P_u. \quad (7)$$

For simplicity, a harmonic oscillation with a single frequency is used in this section

$$a(t) = -A\cdot\sin(2\pi ft), \quad (8)$$

where A is the magnitude of the acceleration, and f is the frequency of the external excitation.

The velocity profile of Poiseuille flow can be described as

$$v(x) = -\frac{\nabla P\lambda^2(s)}{4\mu_w}, \quad (9)$$

where ∇P is the external pressure gradient, r is the radius of the fluid/gas interface, μ_w is the dynamic viscosity of the nonwetting and wetting fluid.

By integrating Eq. (9) in the axisymmetric tube following the lubrication approximation, we obtain the flow rate as

$$Q_1 = -\frac{\pi\nabla P\lambda^4(s)}{8\mu_w}. \quad (10)$$

The total force exerted by the fluid on the capillary wall is given by the following integral:[36]

$$F_x = \int_{L_u}^{s}\tau_i 2\pi\lambda(s)dx, \quad (11)$$

where τ_i is the shear stress at the wetting/nonwetting interface, which is determined by the velocity profile of Eq. (9) and the flow rate Eq. (10)

$$\tau_i = \frac{4\mu_w\langle v_x\rangle}{\lambda(s)}. \quad (12)$$

Substitution of τ_i and Eq. (4) for $\langle v_x\rangle$ into Eq. (11) leads to

$$F_x = -8\pi\mu\lambda^2(s)M1(s)\frac{ds}{dt}, \quad (13)$$

where we define $M1(x)$ as

$$M1(x) = \int_{L_u}^{x}\frac{1}{\lambda^2(\psi)}d\psi. \quad (14)$$

Here, the explicit negative sign ensures physical consistency, indicating that the viscous force acts as a resistive drag opposing the direction of the fluid velocity ds/dt.

According to Eq. (10), the pressure gradient is given as

$$\nabla P_w = -\frac{8\mu_w\lambda^2(s)}{\lambda^4(x)} - \rho a(t). \tag{15}$$

Integrating pressure gradient from plane x = L_u to x gives

$$P(x) = P_u - 8\mu_w\lambda^2(s)\mathrm{M2}(x) - \rho a(t)(x - L_u), \tag{16}$$

where we define $M2(x)$ as

$$M2(x) = \int_{L_u}^{x} \frac{1}{\lambda^4(\psi)}\, d\psi. \tag{17}$$

The pressure force along the constricted wall is

$$F_p = 2\pi \int_{L_u}^{s} P(x)\lambda(x)d\lambda(x). \tag{18}$$

Substituting Eq. (16) into Eq. (18) gives

$$F_p = \pi P_u\left[\lambda^2(s) - \lambda^2(L_u)\right] - 16\pi\mu\lambda^2(s)M3(s)\frac{ds}{dt} - \pi\lambda^2(s)\rho a(t)(s - L_1) + \pi\rho a(t)M4(s), \tag{19}$$

where we define $M3(x)$ and $M4(x)$ as

$$M3(x) = \int_{L_u}^{x} M2(x)\lambda(x)d\lambda(x), \tag{20}$$

$$M4(x) = \int_{L_u}^{x} \lambda^2(\psi)d\psi. \tag{21}$$

According to Beresnev,[18] the oscillatory inertial force in the non-wetting fluid is given by

$$F_a = -\pi\rho a(t)M4(s). \tag{22}$$

The thermodynamic behavior of the gas phase is modeled as an isothermal process governed by Boyle's Law, where the product of the transient gas pressure P_g and bubble volume V_g remains constant (P_gV_g = constant). This assumption is physically justified by the low oscillation frequency (<10 Hz) and the large surface-to-volume ratio of the micro-bubble, which facilitates rapid heat exchange with the surrounding medium. Thus, the state equation is given by

$$P_gV_g = P_g^iV_g^i, \tag{23}$$

where P_g^i and V_g^i are the gas pressure and bubble volume at the initial stationary state.

The hydraulic pressure in domain I near the upstream meniscus P_I is related to the gas pressure in a bubble by the Young–Laplace equation as

$$P_I = P_g - \frac{2\sigma}{\lambda_{men}(s)}, \tag{24}$$

where $\lambda_{men}(s)$ is the radius of curvature of the meniscus at $x = s$, σ is the interfacial tension.

The initial volume of the bubble has three components: two spherical caps and an intermediate cylindrical volume. The volume equation is

$$V_g^i = \pi\int_s^h \lambda^2(x)dx + \frac{2}{3}\pi\lambda^3(s) + \frac{2}{3}\pi\lambda^3(h). \tag{25}$$

At the initial stationary state ($t = 0$), the fluid in domain I is assumed to be static, and the Young–Laplace equation can relate the entrance pressure to the gas pressure by

$$P_g^i = P_u^i + \frac{2\sigma}{\lambda_{men}(s)}. \tag{26}$$

Substitution of Eq. (23) into Eq. (24) gives the transient pressure P_I as

$$P_I = \frac{P_g^iV_g^i}{V_g} - \frac{2\sigma}{\lambda_{men}(s)}. \tag{27}$$

The exit pressure force in the control volume is

$$P_IA_I = \pi\lambda^2(s)P_I. \tag{28}$$

Substitution of Eqs. (6), (7), (13), (19), (22), and (28) into Eq. (2) produces the governing equation in control volume I

$$\rho(s - L_1)\frac{d^2s}{dt^2} = -\rho\left(\frac{ds}{dt}\right)^2 + \frac{4}{3}\rho\frac{\lambda^2(s)}{\lambda^2(x)}\left(\frac{ds}{dt}\right)^2 + \Delta P - 16\mu M3(s)\frac{ds}{dt} - 8\mu M1(s)\frac{ds}{dt} - \rho a(t)(s - L_u), \tag{29}$$

where

$$\Delta P = P_u - \frac{P_g^iV_g^i}{V_g} + \frac{2\sigma}{\lambda_{men}(s)}. \tag{30}$$

D. Momentum balance of downstream fluid in constricted tube

Likewise, the momentum balance of the downstream fluid is established to track the motion of the downstream meniscus of the bubble. The macroscopic governing equation is

$$\rho\frac{d}{dt}\int_V \langle v_x\rangle dV = -\rho A_d\langle v_x^2\rangle + P_{II}A_{II} - P_dA_d + F_p - F_x + F_a, \tag{31}$$

where P_{II} is the hydraulic pressure in the fluid domain II near the downstream meniscus of the bubble. The left-hand side is the rate of momentum change in the control volume. on the right-hand side, $\rho A_d\langle v_x^2\rangle$, $P_{II}A_{II}$, P_dA_d, F_p, F_x, and F_a are momentum efflux at the exit, entrance pressure force, exit pressure force, pressure force along the capillary wall, viscous force along the wall, and oscillatory inertial force, respectively. A_d and A_{II} are the cross-sectional areas of the outlet of the constricted tube and the three-phase contact positions for the upstream meniscus of wetting fluid. P_d and P_{II} are the pressure of the outlet of the constricted tube and three-phase contact positions for the upstream meniscus of wetting fluid.

The modeling approach for fluid domain II follows the same logic as previously discussed. Here, we directly present the momentum balance equation for the bubble, and the detailed derivation can be found in Appendix A

$$\rho\lambda^2(h)(L_d-h)\frac{d^2h}{dt^2}=\rho\lambda^2(h)\left(\frac{dh}{dt}\right)^2-\frac{4}{3}\rho\frac{\lambda^4(h)}{\lambda^2(x)}\left(\frac{ds}{dt}\right)^2+\Delta P\lambda^2(L_d)-16\mu\lambda^2(h)N3(h)\frac{dh}{dt}-8\mu\lambda^2(h)N1(h)\frac{dh}{dt}-\rho\lambda^2(h)a(t)(L_d-h), \tag{32}$$

where

$$\Delta P=\frac{P_g^iV_g^i}{V_g}+\frac{2\sigma}{\lambda_{men}(h)}-P_d, \tag{33}$$

when P_u-P_d is a fixed value, Eqs. (29) and (A17) represent the single-channel model of the bubble.

E. Parallel straight tube

In our model, the straight tube and the contraction tube are parallel and of the same length, so they have the same pressure difference. The sum of the flow rates in the straight tube and the constricted tube is equal to the preset total flow rate, so that we can get

$$Q=Q_1+Q_2, \tag{34}$$

where Q_2 represents the flow rate in the parallel straight tube.

The Hagen–Poiseuille flow equation applies in the straight tube due to its low velocity. Equation (35) describes the relationship between pressure difference and flow rate as follows:

$$Q_2=\frac{\pi r^4}{8\mu_wL}\left(P_u-P_d+\rho_wa(t)\right), \tag{35}$$

where r is the radius of the straight tube. Here, we set the pressure of the outlet to zero.

F. Frequency response function

In a harmonic oscillator, the frequency response function captures important oscillatory characteristics, such as the damping ratio, resonance frequency, and output displacement magnification. Similarly, to describe the oscillation behavior of droplets in this system, the frequency response function can be defined as the ratio of output displacement to input acceleration amplitude. It has the same functionality as the susceptibility function used by Hilpert *et al.*,[20] and is expressed in a dimensionless format:[37]

$$\chi(\omega)=-\frac{\Delta h}{a(\omega)}\omega_c^w, \tag{36}$$

where Δh is the output displacement, and the negative sign arises from the fact that $a(\omega)$ denotes the acceleration of the tube, while the acceleration imposed on the non-wetting fluid is equal in magnitude but opposite in direction. The ω_c^n is the characteristic frequency of the nonwetting phase as defined in Eq. (37). To non-dimensionalize $\chi(\omega)$, as referred to in Hilpert[19]

$$\omega_c^w=\frac{\mu_w}{\rho_w\lambda^2(h)}. \tag{37}$$

During the derivation of the frequency response function, it is assumed that the oscillation amplitude of the bubble is small, making the linear approximation applicable. To rigorously quantify the scope of this approximation, we establish an explicit criterion for its breakdown based on the relative displacement of the meniscus. Following the work of Hilpert,[19] the linear regime is defined by the condition that the dimensionless displacement amplitude satisfies $\Delta h/h_0<1$. When the oscillation amplitude exceeds this threshold ($\Delta h/h_0\geq 1$), the geometric nonlinearity of the capillary force becomes dominant, rendering the linear frequency response functions (derived below) invalid. This criterion will serve as the benchmark for distinguishing between linear and nonlinear responses in the subsequent analysis.

The frequency response functions can be reformulated as

$$\chi^I(\omega)=\frac{1}{\left(X_0^I\right)^2-\left(X_w^I\right)^2\left(\lambda^2(h)\dfrac{\rho_w(L_d-h)+(16\mu_wM3(s)+8\mu_wM1(s))\ i}{\rho_w(L_d-h)\qquad\qquad X_w^I}\right)}, \tag{38}$$

$$\chi^{II}(\omega)=\frac{1}{\left(X_0^{II}\right)^2-\left(X_w^{II}\right)^2\left(\lambda^2(h)\dfrac{\rho_w(L_d-h)+\left(16\mu_wM3(s)+8\mu_wM1(s)+\dfrac{8\mu_wL\lambda^2(s)}{r^4}\right)\ i}{\rho_w(L_d-h+L)\qquad\qquad\qquad X_w^{II}}\right)}. \tag{39}$$

It is important to emphasize that the derivation of the analytical frequency response functions [Eqs. (38) and (39)] is based on the small-perturbation assumption, where the oscillation amplitude of the bubble is significantly smaller than the initial fluid column length ($\Delta h\ll h_0$). Under this condition, the capillary restoring force can be linearized, allowing for the derivation of explicit expressions for natural frequency and damping. The distinct structures of Eq. (38) for the single-channel model and Eq. (39) for the pore-doublet model reflect the fundamental physical differences between the two systems. Specifically, the additional terms appearing in the denominator of the pore-doublet function [Eq. (39)] represent the effective inertial mass and viscous dissipation contributed by the fluid oscillating in the bypass channel. These terms are absent in the single-channel formulation. Consequently, these linear analytical solutions serve to

qualitatively identify how bypass flow modifies the system's intrinsic properties (mass and damping) in the linear limit, rather than to quantitatively predict large-amplitude nonlinear excursions.

The detailed derivation of the frequency response function can be found in Appendix B.

III. METHODOLOGY

To quantify the deviation introduced by neglecting bypass flow in single-channel models relative to the pore-doublet model, we conduct a comparative analysis in both the frequency and time domains. In the frequency domain, we adopt a forced oscillator framework to derive the analytical frequency response functions of the governing equations and compare results across models. In the time domain, we numerically solve the governing equations to obtain the time-dependent bubble displacement $h(t)$ for both models and validate the results against CFD simulations. This section describes the numerical methods used to solve the model equations and outlines the CFD modeling strategy, including the key assumptions, parameter settings, and boundary conditions. The combine analysis enables a systematic assessment of the impact of bypass flow on the bubble dynamics and the fidelity of reduced-order models under vibration excitation.

A. Driven harmonic oscillator

The frequency response function characterizes the natural frequency and damping coefficient of a vibratory system, which are key factors in determining the resonance of a bubble. To investigate how the resonance frequencies of bubbles differ between the two models, we compared their respective frequency response functions. We begin by illustrating the structure of the frequency response function, drawing parallels to the behavior of a harmonic oscillator. The conventional formulation of a driven oscillator is expressed as follows:

$$m\ddot{x} + c\dot{x} + k_0 x = F(t), \tag{40}$$

where x is the time-dependent displacement function of the object, the dot above x indicates the derivative with respect to time, c is the damping, $\omega_0 = \sqrt{k/m}$ is the natural frequency of the system; $F(t)$ is the driving force acting on the system. The acceleration of the object can be calculated as $a(t) = F(t)/m$. When the external driving force is harmonic, the displacement of the object also follows a harmonic form. By transforming the oscillator model in Eqs. (38) and (39) into the frequency domain, the same frequency response function as in Eq. (41) can be applied. Therefore, the form of the frequency response function is

$$\chi(\omega) = \frac{1}{\mathrm{X}_0^2 - \mathrm{X}_n^2\left[1 + \frac{c\,i}{m\omega}\right]}, \tag{41}$$

where $\chi(\omega)$ is a complex number, and its absolute value $|\chi(\omega)|$ represents the ratio of output displacement to input acceleration, while the relative magnitudes of the imaginary and real parts indicate the phase angle between the output displacement and input acceleration. Resonance occurs when the peak of $|\chi(\omega)|$ is located at a non-zero frequency. In Eq. (41), the coefficient of X_n^2 is a complex number, with the real part representing the mass term and the imaginary part representing the damping term. This information will be used to compare the frequency response functions of the two models.

B. Numerical solution procedure for the theoretical model

Equations (29), (32), (34), and (35) are coupled together to solve for the transient values of s and h, as well as the pressure and flow rate within the constricted tube. Equations (29) and (32) represent initial value problems, requiring appropriate initial conditions to fully define the system. Initially, the bubble is assumed to be trapped at the constriction, meaning that all fluid flow occurs in the straight tube. The initial conditions are as follows:

$$h(0) = h_0, \tag{42}$$

$$s(0) = s_0, \tag{43}$$

$$\frac{dh(0)}{dt} = 0. \tag{44}$$

A fourth-order Runge–Kutta method is employed to integrate Eqs. (29) and (32) in time. The Gaussian quadrature with 16 points is used to evaluate the integrals in Eqs. (14), (17), (20), (21), (A3), (A7), (A10), and (A11). The time step is set to 5×10^{-5}. The pressure drop $P_u - P_d$ is first determined from Eqs. (34) and (35) as the bubble is trapped at the constriction. With known pressure drop, the downstream contact line h can be updated by solving Eqs. (4) and (14). The geometric parameters and fluid properties are $r_{min} = 0.5$ mm, $r_{max} = 2.5$ mm, $L = 10$ mm, $L_u = -20$ mm, $L_d = 20$ mm, $h_0 = -0.6299$ mm, $s_0 = -15$ mm, $\rho_w = 1000$ kg/m^3, $\mu_w = 0.001$ Pa s. The total flow rate $Q = 2.3 \times 10^{-9}$ m^3/s, $r = 0.8$ mm, $L = 40$ mm. The contact angle of the wetting phase is set to 0°.[21]

C. CFD modeling

The two-phase Navier–Stokes equations are solved using the volume of fluid (VOF) method within the finite volume framework in FLUENT, and the results are compared with theoretical models, including both single-channel and pore-doublet models. The Navier–Stokes equations describe the dynamics of each fluid phase individually

$$\begin{cases} \rho\dfrac{\partial}{\partial t}\vec{v} + \rho\nabla(\vec{v}\vec{v}) = -\nabla P + \mu\nabla(\nabla\vec{v} + \vec{v}^T) + \vec{F} \\ \nabla\vec{v}, \end{cases} \tag{45}$$

where $\vec{v}$ is the velocity vector; ρ is the density of fluid; μ is the viscosity of fluid; P is the static pressure; $\vec{F}$ is the body force. The VOF method is used to describe two-phase flow. In the VOF approach, the parameters ρ and μ in Eq. (45) represent the volume-fraction-weighted density and viscosity, respectively, within each computational cell. The body force considered in this study is the sum of the volumetric surface force and the oscillatory body force

$$\vec{F} = \sigma\kappa\nabla\alpha_n - \rho a(t), \tag{46}$$

where κ is the curvature of the interface; α_n is the volume fraction of the nonwetting phase. In this study, the VOF method is used to model the two-phase flow, where the non-wetting fluid was defined as the secondary phase and assigned a value of 1.

Because of the inherent difficulty in directly tracking the leading edge of the bubble within CFD simulations, we develop a computer vision-based post-processing method to extract the front interface

position with high fidelity. This method involves applying color masking to isolate the red and blue channels that represent the bubble, followed by Gaussian filtering to suppress image noise. The front interface is then identified by computing the indices of non-zero columns in the filtered images, allowing precise localization of the bubble's contact point. A detailed pseudocode description of the image-processing pipeline is provided in the Supplementary Material.

While conventional single-channel CFD models can accommodate fixed pressure differences, modeling the pore-doublet geometric structure requires a more complex challenge due to the inherently time-dependent boundary pressures. To overcome this limitation, we design a custom boundary control strategy using a user-defined function (UDF) embedded in the CFD solver. This approach dynamically adjusts the boundary pressure based on a theoretically derived model, enabling accurate simulation of the dual-tube system. The derivation of the pressure boundary model and the corresponding UDF logic are both detailed in the Supplementary Material.

Given the high computational cost of transient VOF simulations, which require resolving dynamic contact lines with varying time steps, we adopt a strategic sampling approach for quantitative validation rather than a continuous spectral sweep. The CFD simulations are conducted at selected critical frequencies to benchmark the theoretical model across three distinct dynamic regimes: the low-frequency limit (e.g., 1 Hz), to validate the model's handling of quasi-static capillary restoring forces and viscous dissipation; the high-frequency limit (e.g., 10 Hz), to verify the inertial terms and dynamic coupling effects when acceleration dominates; and the resonance region, where we perform dense frequency sampling around the predicted resonance peaks to rigorously test the model's ability to capture maximum oscillation amplitudes and frequency shifts. This multi-point validation strategy, applied under both small-amplitude and large-amplitude excitations, ensures that the theoretical model is quantitatively accurate in capturing the key physics of the system.

The UDF employs an explicit coupling scheme, updating the boundary pressure based on flow data from the previous time step. This can introduce numerical pressure oscillations (artifacts) if the time step is large. In this study, a time step of 5×10^{-5} s was strictly enforced to minimize this coupling latency. Additionally, the UDF assumes incompressible pressure transmission through the bypass channel, neglecting acoustic propagation delays, which is a valid assumption for the low-frequency range (1–10 Hz) considered here.

IV. RESULTS

We compare the single-channel model and the pore-doublet model from both frequency-domain and time-domain perspectives. The frequency-domain analysis, based on linearized approximations, is limited to small-amplitude oscillations but explicitly incorporates pressure redistribution caused by the bypass channel. In contrast, the time-domain analysis does not rely on linearization and, when combined with CFD simulations, captures large-amplitude oscillations and nonlinear coupling effects associated with bypass flow. Building on these analyses, we evaluate the influence of bypass flow on key dynamic characteristics, including resonance frequency, damping, and mobilization thresholds. We further quantify the physical significance of discrepancies between the linear frequency-domain results and the nonlinear time-domain responses.

A. Comparison in the frequency domain

The frequency response functions from the two models, as shown in Eqs. (38) and (39), are explicit. In these equations, the term $\chi(\omega)$ in the denominator represents the dimensionless natural frequency, while the second term, in complex form, indicates the damping coefficient. The resonance frequency of the bubble is determined by both the natural frequency and the damping coefficient.

To better interpret the expression for the natural frequency, we draw an analogy to the classical harmonic oscillator. The natural frequency of a harmonic oscillator can be expressed as $\omega_0 = \sqrt{k/m}$. In the present model, the coefficient $2\sigma f(\beta, \wedge, x^*)/r^2{}_{min}$ in Eq. (B9), derived from the linearization of capillary forces,[19] plays a role analogous to the spring constant k, The remaining term within the square root is the inverse of the effective fluid mass, analogous to $1/m$. Notably, the effective fluid mass differs fundamentally between the two models, as revealed by the analytical expressions for natural frequency derived in Appendix B. By comparing Eq. (B12) for the single-channel model and Eq. (B13) for the pore-doublet model, we can explicitly decompose the inertial contributions.

In the single-channel model, the effective mass term in the denominator is proportional to $\rho_w(L_d - h)$, which corresponds strictly to the inertia of the downstream fluid column within the constricted tube. In contrast, the pore-doublet model contains an additional inertial term, resulting in an effective mass proportional to $\rho_w(L_d - h + L)$. Here, the term $\rho_w L$ represents the explicit contribution of the fluid mass within the bypass channel to the system's total inertia. Since the natural frequency scales with the inverse square root of the effective mass ($\omega_0 \propto M_{eff}^{-1/2}$), the mathematical inclusion of this bypass inertial term ($\rho_w L$) directly explains the reduction in resonance frequency observed in the pore-doublet model.

As illustrated in Fig. 1(b), the single-channel model considers only the wetting fluid slug in the constricted tube. However, under vibration, fluid in the bypass channel also oscillates. This bypass flow contributes to the system's inertia and must be included in the effective mass term for accurate natural frequency computation. Accurate characterization of the oscillatory behavior of immiscible fluids thus requires incorporating the full mass of all dynamically coupled fluid components.

The damping terms in the denominator of the frequency response function are also compared. In the pore-doublet model, damping arises from multiple sources: viscous forces acting on the wetting fluid segments within the constricted tube, wall-induced pressure losses, inertial effects associated with oscillating immiscible fluids, and pressure drops across the bypass flow path. In contrast, the single-channel model neglects the contribution of the bypass flow and associated dissipation mechanisms. As a result, it systematically underestimates the total damping of the system, leading to inaccuracies in the predicted amplitude and phase of the frequency response.

The frequency response function quantifies the relationship between the output displacement amplitude of the nonwetting droplet and the input acceleration under vibration excitation. Using the geometric and fluid parameters specified in Sec. III B, we compute the absolute values of the frequency response functions for both models (Fig. 3). Under the given conditions, both models exhibit underdamped behavior, with well-defined resonance peaks observed at approximately 3.6 Hz for the single-channel model and 2.6 Hz for the pore-doublet model. The single-channel model yields sharper and

higher resonance peaks compared to the pore-doublet model, indicating a lower effective damping. This is consistent with the previous analysis of damping contributions. The qualitative features of the response curves, particularly the steepness near resonance, serve as indicators of system damping. A steeper slope around the resonance frequency reflects reduced energy dissipation. The broader and flatter peak in the pore-doublet model thus suggests enhanced damping due to bypass flow and associated viscous losses.

These results confirm that incorporating bypass flow alters the system's effective oscillating mass and enhances overall damping via additional shear forces and pressure perturbations. Consequently, the pore-doublet model offers a more accurate representation of bubble dynamics than the single-channel model, which overestimates resonance frequency and amplitude by neglecting these mechanisms. These findings highlight the necessity of explicitly incorporating bypass flow effects in theoretical modeling to improve predictive fidelity.

B. Comparison in time domain

The amplitude of bubble oscillations is strongly influenced by proximity to microseismic sources or other vibrational energy inputs. To capture this amplitude-dependent behavior, we compare the two models under small-amplitude and large-amplitude excitations separately. For small-amplitude excitations, the results from time-domain simulations are consistent with those obtained from linearized frequency-domain analysis. However, when the relative displacement becomes large (i.e., $\Delta h/h_0 > 1$), the linear approximation of capillary forces with respect to Δh becomes invalid. In this regime, the full nonlinear governing equations must be solved to capture the bubble dynamics accurately. Large-amplitude oscillations exhibit strong nonlinear behavior, and the associated displacements $h(t)$ lead to significant deviations from the linear model predictions. As a result, linearized formulations become inadequate for modeling bubble mobilization under large-amplitude excitation.

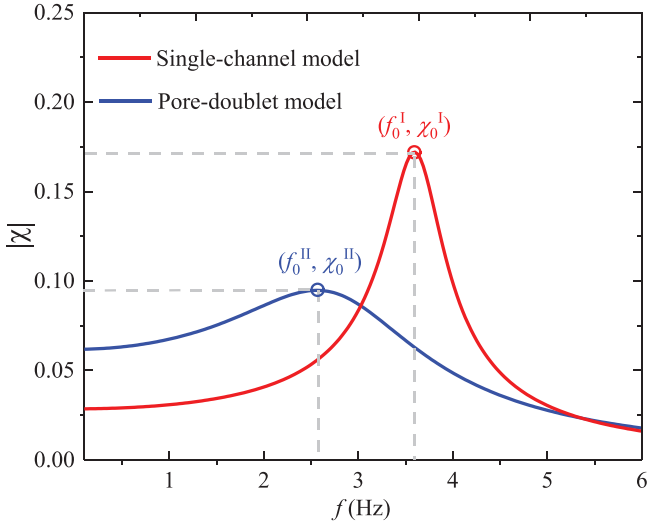

FIG. 3. The absolute value of the frequency response function in the two models. The peak ratio and the associated resonant frequency are marked by the circle at the coordinate in the plot. The theoretical results were acquired from 200 points in the interval between 0.1 and 6 Hz.

1. Small-amplitude excitation

This subsection investigates the linear response behavior under low-amplitude vibrational forcing and compares model predictions with direct numerical simulations. We begin by examining the response of the system under small-amplitude excitations. The governing equations are numerically solved to quantify the oscillation of the non-wetting droplet in the time domain. To facilitate analysis, we define the amplification ratio, which is similar to the frequency response function, as

$$\xi = \frac{|h(t)|}{|a(t)|}\left(\omega_c^{\omega}\right)^2, \tag{47}$$

where ξ is a dimensionless variable. The parameters used to calculate ξ are referenced in Sec. III B. The amplitude of acceleration is $A = 0.01\ \mathrm{m/s^2}$.[37]

To validate the theoretical framework, time-domain CFD simulations are performed under identical excitation conditions. First, to explicitly visualize the underlying fluid dynamics, Fig. 4 presents the spatiotemporal evolution of the phase distribution and velocity field over a single oscillation period (T). As shown in the velocity streamlines, the fluid exhibits periodic flow reversal and localized vortices within the constricted tube, driving the oscillatory deformation of the bubble. Quantitative comparisons of the displacement $h(t)$ are shown in Fig. 5. It should be noted that CFD simulations are conducted at selected representative frequencies to capture key dynamic regimes. Under small-amplitude excitation ($A = 0.01\ \mathrm{m/s^2}$), the results are verified for both the boundary frequencies (1 and 10 Hz) and the predicted resonance frequencies (approximately 2.6 Hz for the pore-doublet model and 3.6 Hz for the single-channel model). The oscillatory motion obtained from both the theoretical model and CFD simulations consists of two distinct stages: an initial transient stage and a steady-state stage. The transient stage is primarily influenced by initial conditions and dissipative effects, gradually decaying over time, while the steady-state response emerges once the system reaches dynamic equilibrium. Therefore, in this study, we focus primarily on the steady-state response, as it effectively characterizes the resonance behavior of the system.

The theoretical models reproduce both the amplitude and phase observed in the CFD simulations with minimal discrepancy in the steady-state regime, supporting the validity of the theoretical model. Minor discrepancies observed in the transient stage, limited to the initial few cycles, are attributed to differences in the treatment of viscous forces within the convergent–divergent section. Since the transient oscillation consists of both forced and free modes and is highly sensitive to damping, it is not discussed in detail here.

Figure 6 presents the time-domain comparison between the single-channel model and the pore-doublet model. Under the specified parameter conditions, both models exhibit resonance, with corresponding resonance frequencies of 3.6 Hz for the single-channel model and 2.6 Hz for the pore-doublet model. These results are consistent with those from the frequency-domain analysis, confirming that the system remains within the linear response regime at the current excitation level.

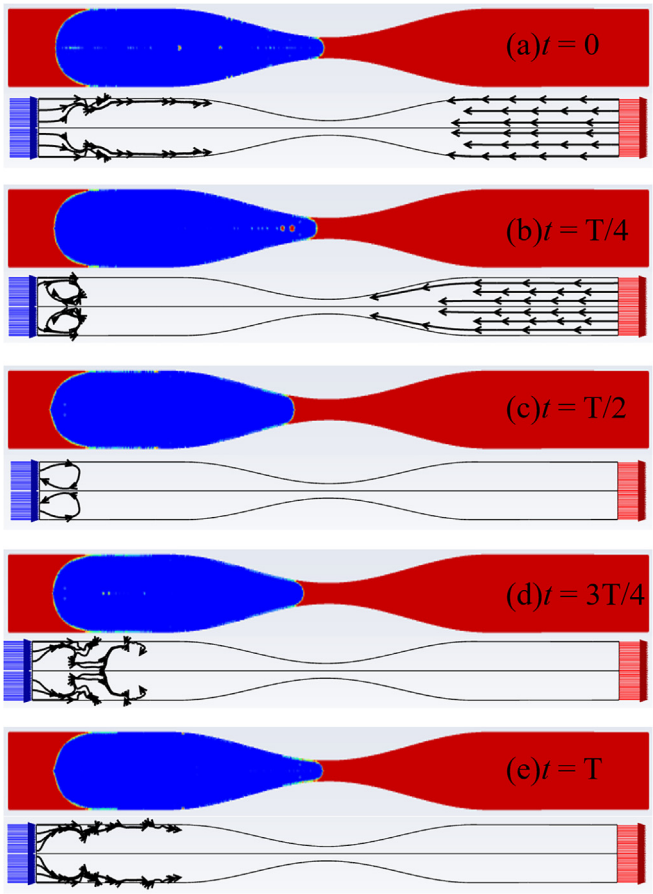

FIG. 4. Spatiotemporal evolution of bubble morphology and flow field characteristics over a single vibration period. The subplots (a)–(e) correspond to five key instants: $t = 0$, T/4, T/2, 3 T/4, and T. In each panel, the upper part displays the phase distribution contours (blue represents the gas bubble, red represents the wetting liquid), showing the periodic extension and retraction of the interface. The lower part visualizes the corresponding velocity streamlines and vector fields within the constricted tube. These streamlines clearly illustrate the periodic flow reversal and the formation of transient vortices near the menisci driven by the oscillatory inertial forcing.

However, it is noteworthy that the resonance amplitudes observed in the time-domain responses are substantially lower than those predicted by the frequency-domain analysis. This discrepancy primarily arises from methodological differences: the time-domain response is obtained by solving the governing differential equations, explicitly accounting for damping effects. Even within the linear regime, damping reduces oscillation amplitudes during the transient phase. In contrast, frequency-domain analysis typically assumes the system has reached a steady state and neglects energy dissipation during transients, thereby overestimating the resonance peak.

More importantly, the observed differences in resonance frequency and amplitude between the two models reflect fundamental changes in system dynamics induced by the presence of bypass flow. Compared to the single-channel model, the pore-doublet model explicitly incorporates the influence of the bypass channel, introducing additional fluid mass and viscous dissipation terms. The inertial contribution from fluid in the bypass path lowers the system's effective natural frequency, while the associated viscous resistance increases overall system damping. These coupled effects manifest as reduced resonance frequency and attenuated amplitude, as observed in both frequency- and time-domain results. This highlights the physical relevance of bypass flow in governing bubble oscillation dynamics and underscores its importance in realistic modeling of partially saturated porous media.

2. Large-amplitude excitation

Under large-amplitude excitation conditions, we first consider the scenario where the bubble remains trapped and does not cross the pore throat. To isolate this behavior, we select an appropriate excitation amplitude to ensure the bubble remains pinned throughout the vibrational forcing. After iterative calibration, we choose an excitation amplitude of 0.1 m/s^2. As in the small-amplitude analysis, we compare the theoretical model with CFD simulations for both models at $A = 0.1$ m/s^2 (Fig. 7). The results show that under large-amplitude excitation, the theoretical model still captures the dynamic response observed in the CFD simulations. Figure 8 shows the relationship between the system's amplification factor and frequency. The results indicate that both the single-channel model and the pore-doublet model exhibit resonance. However, in contrast to the small-amplitude case, we observe a clear resonance softening effect, with the resonance peak shifting to lower frequencies. Specifically, the resonance frequency decreases from 3.6 to 3.4 Hz for the single-channel model, and from 2.6 to 1.9 Hz for the pore-doublet model. This frequency shift indicates that the system enters the nonlinear response regime.[38]

To rigorously validate these theoretical predictions, especially the amplitude-dependent resonance offset, we performed transient CFD simulations and dense frequency sampling around the formants. Figures 9 and 10 show detailed time-domain comparisons of single-channel and aperture dual-state models, respectively. Quantitative analysis of the steady-state response showed excellent agreement between the CFD results (red dotted line) and the theoretical predictions over the linear interval at small excitation amplitudes ($A = 0.01$ m/s^2). Specifically, the relative error of steady-state amplitude remains low at linear resonance frequencies (3.6 Hz for the single-channel model and 2.6 Hz for the pore-doublet model), averaging about 1.6%, and the phase difference is negligible ($\Delta\varphi < 2°$). These results confirm that the linear model accurately captures viscous damping and effective inertia. For the nonlinear interval ($A = 0.1$ m/s^2), the predicted frequency offset was verified, and the CFD simulation showed that the maximum amplitude response of the pore bimorphism model dropped to 1.9 Hz with a relative error of 7.3%. This high deviation is due to the chaotic interface fluctuations and complex bypass coupling captured by the VOF method, which has been simplified in the theoretical model. Similarly, the resonance frequency of the single-channel model is directed toward 3.4 Hz with a relative error of 4.1%. Even in the nonlinear interval, the phase hysteresis maintains a good boundary ($\Delta\varphi < 6°$), indicating that the theoretical model correctly scales the energy dissipation of the system. Together, these indicators show that the proposed framework effectively captures the "softening" of rigid and nonlinear damping mechanisms, providing a robust prediction tool for bubble dynamics at different excitation levels.

The nonlinear time-domain model captures this frequency drift and dynamic behavior more accurately than the frequency-domain

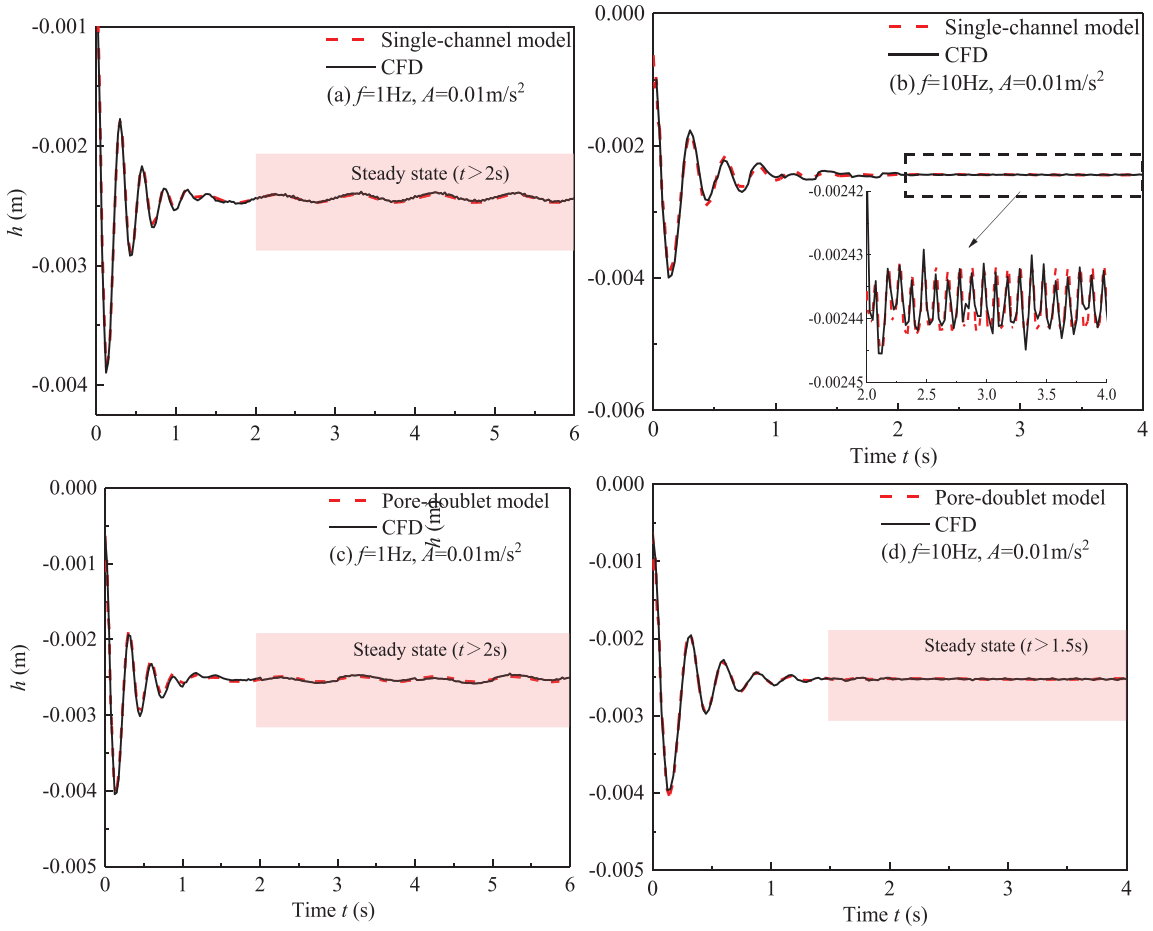

FIG. 5. Comparative validation of the theoretical displacement response h(t) under small-amplitude excitation ($A = 0.01$ m/s^2). (a) and (b) show the comparison between the single-channel model and CFD at excitation frequencies of 1 and 10 Hz, respectively; in (b), the arrow marks the region where a magnified inset is provided. (c) and (d) present the corresponding results for the pore-doublet model at 1 and 10 Hz. In all cases, the dashed red line represents the theoretical model prediction, and the solid black line represents the CFD simulation result.

response function model, which relies on linear assumptions and cannot reliably describe such nonlinear changes. In the nonlinear regime, the influence of bypass flow on the system's characteristics becomes increasingly significant. During large-amplitude bubble oscillations, fluid exchange continues to occur through the bypass path in the pore-doublet model, causing variations in both the effective mass and viscous dissipation terms with amplitude. This nonlinear coupling introduced by bypass flow results in a more pronounced frequency shift and stronger attenuation of the resonance peak in the pore-doublet model compared to the single-channel model. As a result, the resonance response becomes more subdued, with increased damping. Although both models exhibit resonance softening, the contribution of bypass flow to damping and energy dissipation is notably stronger under high-amplitude excitation, further suppressing the bubble's resonance amplification. These findings suggest that once the system enters the nonlinear regime, bypass flow not only alters the frequency response profile but also delays the onset of instability or bubble mobilization.

Additionally, we compare the critical amplitude A_{crit} at which the system transitions from linear to nonlinear behavior for both models as the oscillation amplitude increases. In the linear regime, changes in amplitude do not alter the shape of the frequency response function but only amplify the response,[39,40] with results similar to those obtained from frequency-domain analysis.[41] However, once the excitation amplitude exceeds A_{crit}, the frequency response function changes, and resonance frequency shifts, chaotic behavior, and other phenomena emerge. The onset of nonlinearity leads to instability in the system. Therefore, identifying A_{crit} is important for ensuring safety in practical engineering applications. We define the critical amplitude as the excitation amplitude at which the absolute frequency shift of the resonance frequency relative to the linear system exceeds 2%.

As the excitation amplitude increases, we observe a significant change in A_{crit}. As shown in Fig. 11, with increasing excitation amplitude, the frequency response function exhibits a notable change. At low amplitudes, the system behaves linearly, and the frequency response curve shows linear amplification. However, once the

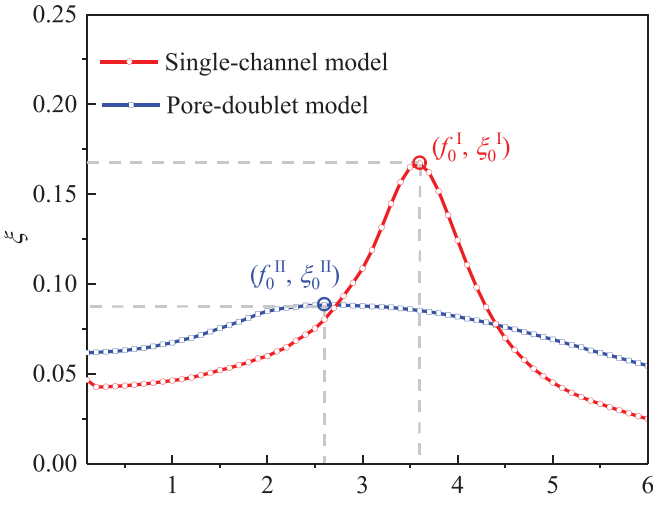

FIG. 6. Comparison of the frequency response curves for the single-channel model and the pore-doublet model under small-amplitude excitation ($A = 0.01$ m/s^2). The peaks of the frequency response curves for both models are marked, defined as the resonance frequency f_0 and resonance peak ξ_0. Under small-amplitude excitation, the resonance frequencies for the two models are 2.6 and 3.6 Hz, respectively. The fluid properties are $\sigma = 0.045$ N/m, $\rho_w = 1000$ kg/m3 $\mu_w = 0.001$ Pa s.

amplitude reaches a critical value, the frequency response curve undergoes a substantial change, with resonance frequency shifts and peak attenuation typical of nonlinear behavior. Figures 11(a) and 11(b) show the responses of the pore-doublet and single-channel models under different excitation amplitudes.

Figure 12 illustrates that the pore-doublet model enters the nonlinear stage at a lower excitation amplitude (0.04 m/s^2), while the single-channel model requires a higher excitation amplitude (0.08 m/s^2). This difference indicates that the pore-doublet model exhibits nonlinear characteristics at lower excitation levels. To theoretically substantiate the observed resonance softening, we analyze the capillary restoring force in the governing equations [Eqs. (29) and (32)], noting that the pore constriction is geometrically defined by a cosine function [Eq. (1)]. Since the capillary pressure is determined by the local radius [$P_c \propto 1/\lambda(x)$] and the restoring force arises from the pressure gradient [$F_{cap} \propto -(\partial P_c/\partial x)$], the restoring force is mathematically proportional to the spatial derivative of the pore radius. Consequently, the derivative of the cosine-shaped geometry yields a restoring force that follows a sine function of displacement [$F_{cap} \propto \sin(kx)$]. By performing a Taylor series expansion of this sinusoidal force around the equilibrium position, we obtain a form analogous to the Duffing oscillator, $F_{cap} \approx \alpha x - \gamma x^3$, where the linear term (αx) represents the small-amplitude stiffness. Crucially, the cubic term stems from the third-order expansion of the sine function ($\sin\theta \approx \theta - \theta^3/6$), resulting in a naturally negative coefficient ($-\gamma$, corresponding to $\beta < 0$ in the standard Duffing equation). This mathematical derivation rigorously proves that the restoring force increases less than linearly as the bubble moves into the wider sections of the pore, thereby reducing the effective stiffness and causing the downward frequency shift (softening) observed in the large-amplitude regime.

Further analysis attributes the earlier onset of nonlinear behavior in the pore-doublet model to bypass flow. As excitation amplitude increases, the bypass channel introduces complex fluid pathways that modify the system's effective mass and damping. This nonlinear coupling accelerates the transition to nonlinearity compared to the single-channel model, demonstrating the critical role of bypass flow in modulating system stability.

As the excitation amplitude increases further, the bubble meets the previously defined mobilization criterion, overcoming the capillary resistance and passing through the pore throat under oscillatory forcing. Before analyzing the critical mobilization behavior in detail, it is necessary to clarify the flow assumptions and boundary conditions adopted in this study. We assume Poiseuille flow as the velocity profile within the channels, which requires a finite time to fully develop. According to Deng and Cardenas,[21] the time required to establish a complete Poiseuille velocity profile should be comparable to the oscillation period; otherwise, the flow will not fully develop, compromising the accuracy of momentum transfer. Based on this consideration, we set the frequency range in this study to 1–10 Hz to ensure that the velocity profile can fully develop within each oscillation cycle.

With further increases in excitation amplitude, the previously trapped bubble eventually becomes mobilized. We define the critical mobilization acceleration, A_c, as the minimum vibration acceleration required for the bubble to overcome the pore throat constraint. Within the selected frequency range, a comparative analysis of A_c under the single-channel model and the pore-doublet model is presented in Fig. 13. The results show that A_c does not increase monotonically with frequency under resonant conditions. Instead, it exhibits a non-monotonic, phase-dependent nonlinear behavior. Initially, as frequency decreases, both models show an increase in A_c, due to shorter vibration cycles at higher frequencies, which reduce the effective force applied per unit time and therefore require larger acceleration amplitudes to achieve mobilization. However, once the excitation frequency enters the resonance range, both models exhibit a decreasing trend in A_c, indicating that the enhanced oscillation amplitude associated with resonance facilitates bubble mobilization.

More importantly, differences are observed not only in the magnitude of A_c between the two models, but also in their respective resonance frequency ranges: the single-channel model exhibits resonance at 6–7 Hz, while the pore-doublet model resonates at 7–8 Hz. This discrepancy arises from nonlinear coupling in the pore-doublet model, where fluid in the bypass channel creates an additional dynamic pathway. This coupling varies the system's effective mass and damping with frequency, increasing sensitivity and lowering critical mobilization thresholds under resonant conditions. Furthermore, bypass flow enhances pressure redistribution and capillary pressure differentials under vibrational forcing, accelerating interface deformation and thereby further reducing A_c.

These findings highlight the crucial role of bypass flow in dictating nonlinear bubble dynamics under vibrational forcing. Accurate prediction of bubble mobilization in porous systems, therefore, requires explicit modeling of the coupled dynamics between primary and bypass flow paths.

C. Effect of permeability on resonance frequency

To demonstrate the robustness of the resonance frequency reduction caused by bypass inertia, we analyzed the system response under varying permeability conditions. By varying the geometric parameters of this equivalent channel, we perform a sensitivity analysis to quantify

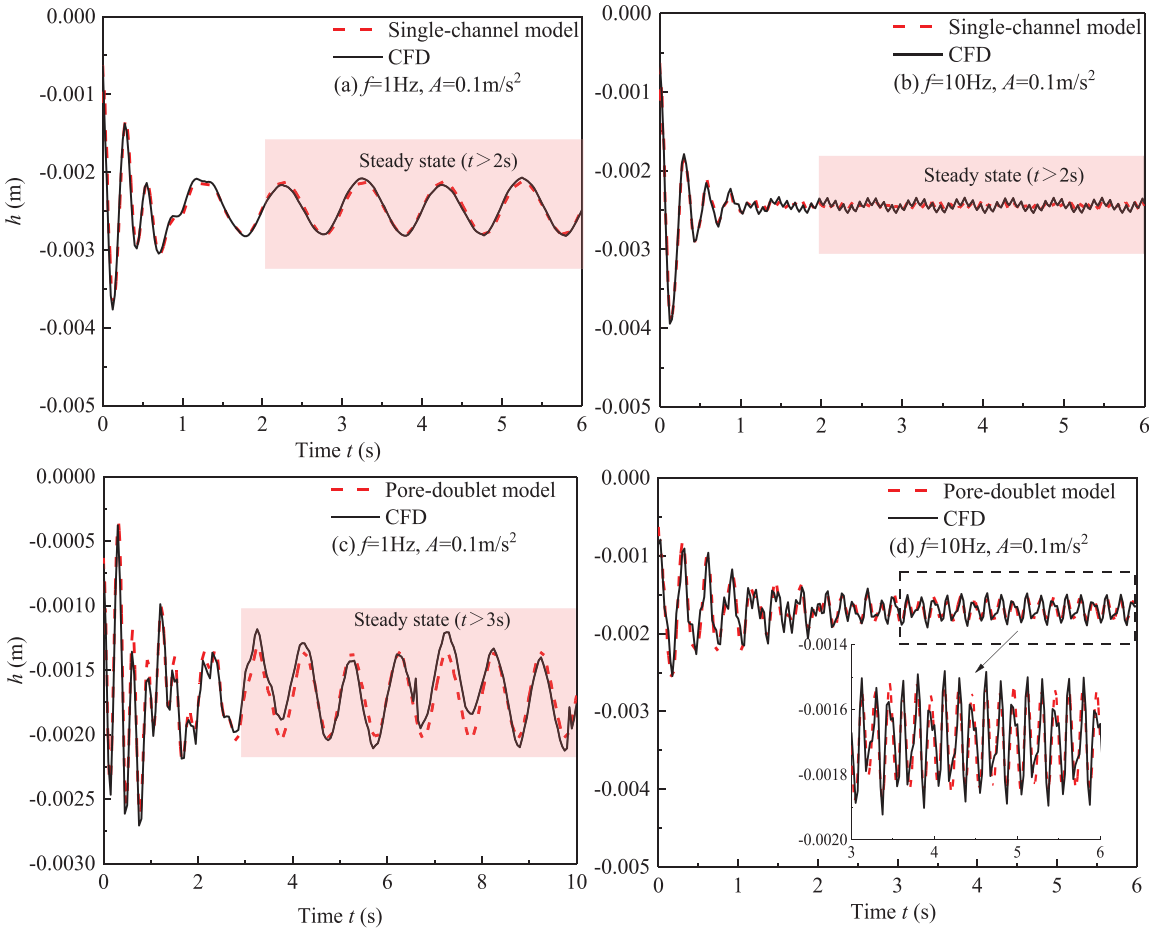

FIG. 7. Comparative validation of the theoretical displacement response $h(t)$ under large-amplitude excitation ($A = 0.1\ \mathrm{m/s^2}$). (a) and (b) show the comparison between the single-channel model and CFD at excitation frequencies of 1 and 10 Hz, respectively; (c) and (d) present the corresponding results for the pore-doublet model at 1 and 10 Hz; in (d), the arrow marks the region where a magnified inset is provided. In all cases, the dashed red line represents the theoretical model prediction, and the solid black line represents the CFD simulation result.

how the hydraulic properties of the bypass path, representing different degrees of pore connectivity, alter the resonance frequency and amplitude. The permeability of each tube is estimated using the classical circular tube formula, $k = r^2/8$, where r is the tube radius. This configuration allows for a parametric investigation of how effective permeability influences the vibrational response of trapped gas bubbles under vibration excitation. The radii of the straight tubes are set to $r = 0.6$, 0.7, and 0.8 mm, respectively, corresponding to permeabilities of 45.6, 62.0, and 81.1 mD, respectively. At the same time, we need to ensure that the initial position of the bubble remains unchanged. Therefore, according to the Poiseuille flow criterion, the initial flow rates corresponding to the three permeabilities are as follows: 2.3×10^{-9}, 4.31×10^{-9}, and $7.20 \times 10^{-9}\ \mathrm{m^3/s}$.

As shown in Fig. 14, under three k conditions, the frequency response function of the bubbles exhibits consistent characteristics. While the added effective mass from the bypass flow ($\rho_w L$) fundamentally lowers the natural frequency compared to the single-channel model, the specific resonance value is altered by the viscous damping. As k increases, the time response curve shifts to the right, with both resonance frequency and peak amplitude increasing. According to the damping term in Eq. (39), a larger channel radius reduces system damping, which in turn increases both resonance frequency and peak. At low k (e.g., $k = 45.6$ mD in this study), the secondary resonance peak is particularly prominent, with a frequency of approximately 1.5 Hz, which is close to half of the primary resonance frequency (3.1 Hz). This result aligns with the findings of Prosperetti *et al.*[41] However, as k increases, the secondary resonance peak gradually weakens and eventually disappears, while the primary resonance peak becomes more pronounced. This phenomenon may be attributed to the high internal flow resistance in porous media with low k. The increased resistance complicates and slows fluid flow patterns, enabling greater energy accumulation in the secondary resonance mode and resulting in higher amplitudes. Under nonlinear vibration conditions, low-frequency secondary resonance modes may dominate energy distribution, making them more prominent compared to high-frequency primary resonance modes.

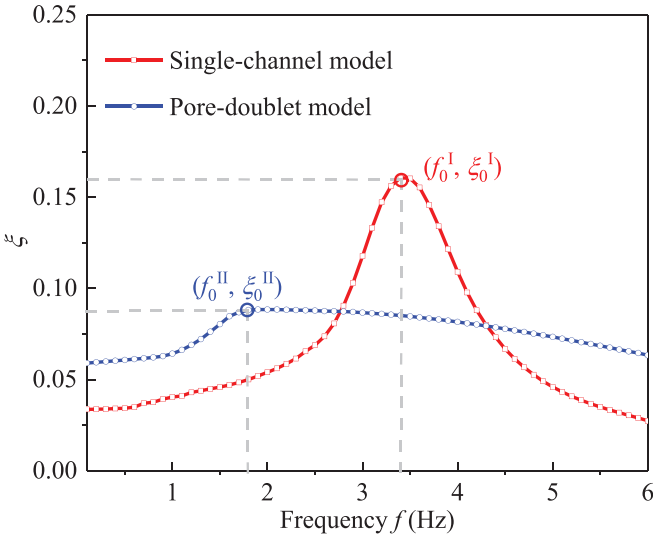

FIG. 8. Comparison of the frequency response curves for the single-channel model and the pore-doublet model under large-amplitude excitation ($A = 0.1$ m/s^2). The peaks of the frequency response curves for both models are marked, defined as the resonance frequency f_0 and resonance peak ξ_0. Under large-amplitude excitation, the resonance frequencies are 1.9 and 3.3 Hz, respectively. The fluid properties are $\sigma = 0.045$ N/m, $\rho_w = 1000$ kg/m3 $\mu_w = 0.001$ Pa s.

An intriguing and insightful phenomenon observed in this study is the distinct behavior of gas bubbles and oil droplets under secondary resonance conditions. Previous studies have shown that the secondary resonance peaks of oil droplets typically appear on the right-hand side of the primary peak and often correspond to integer multiples of the fundamental frequency.[42] This contrast arises from the fundamental differences in their physical properties. Oil droplets, as homogeneous liquid bodies, possess uniform density and elastic characteristics. Their vibrational dynamics are primarily governed by surface tension and internal viscous flows, resulting in more regular and predictable resonance behavior. In contrast, gas bubbles exhibit pronounced compressibility, heterogeneous phase interfaces, and more complex fluid-structure interactions, leading to fundamentally different resonance characteristics.[43,44] In contrast, gas bubbles possess a complex gas-liquid interfacial structure, and their vibrational behavior is strongly influenced by interfacial coupling and nonlinear effects. As a result, their secondary resonance frequencies are typically lower than those of oil droplets.[45,46] A deeper understanding of these physical characteristics is critical for a wide range of industrial and natural processes, including emulsion stability, flotation technologies, microfluidic device operation, and ultrasonic imaging.[47–50]

Although similar phenomena have been noted in previous studies, a systematic investigation of permeability-dependent vibrational behavior remains absent. The present work offers new insights into the evolution of secondary vibrational modes under varying permeability conditions, contributing to a more comprehensive understanding of nonlinear bubble dynamics in porous media. It is important to note that the permeability values employed here are derived from an idealized circular capillary model. While such geometric simplifications may not fully capture the structural complexity of natural porous media, they provide a tractable theoretical framework to isolate and examine the effects of effective permeability on vibrational response and bubble mobilization trends.

V. DISCUSSION

A. Bypass flow modulates nonlinear bubble oscillations

While prior studies have primarily focused on incompressible droplets to model two-phase flow in porous media,[18,19,21] the dynamics of compressible gas bubbles under vibration remain far less understood. Compared to droplets, gas bubbles exhibit pronounced resonance behavior, strong inertial coupling, and highly deformable interfaces, particularly under large-amplitude excitation. In this context, momentum-based models, as advocated by Zeng and Deng,[37] are more appropriate than traditional pressure or force balance formulations due to their ability to capture nonlinear dynamics. For instance, Christov *et al.*[51] demonstrated that inertia-induced displacement mechanisms are distinct from capillary entrapment, which corroborates our finding that bypass flow alters the system's effective inertia.

The present work extends this momentum framework by introducing a pore-doublet model that explicitly accounts for bypass flow, an element that is absent in most conventional representations. Our results demonstrate that bypass flow introduces three dominant mechanisms: (i) pressure redistribution damping, where time-lagged pressure gradients resist bubble motion; (ii) shear-induced viscous dissipation within the bypass conduit; and (iii) dynamic mass coupling due to fluid inertia. Collectively, these mechanisms significantly alter the oscillatory behavior of bubbles, reducing resonance amplitudes and shifting resonance frequencies.

However, the influence of bypass flow is not limited to modifying dynamic response; it also has implications for how bubbles unlock and mobilize under subcritical forcing. Our results show that bypass flow facilitates capillary pressure modulation, thereby lowering the mobilization threshold. These insights challenge simplified models that treat surrounding fluid regions as passive and suggest that local pore-scale heterogeneities play an active role in controlling bubble dynamics.

Despite these advances, several limitations warrant consideration. First, the pore-doublet geometry employed here, while analytically tractable, cannot fully capture the topological complexity of natural porous networks. For instance, in three-dimensional systems, tortuosity and interconnectivity may result in multipath bypassing, with different phase lags and dissipation scales. Second, the assumption of Poiseuille flow neglects inertial effects near pore constrictions and interface instabilities that may arise under high-frequency excitation. Future studies may benefit from extending the model to more realistic pore networks, incorporating stochastic distributions of throat sizes and orientations.

Comparing our resonance frequencies with previous studies highlights the critical role of compressibility: while droplets typically resonate above 6 Hz,[37] the resonance frequencies predicted for gas bubbles here fall within the 2–4 Hz range. This suggests that previous droplet-based models may overestimate system stiffness and underestimate dissipation in gas-invaded porous media. Consequently, these findings may have broader implications for modeling geophysical processes, such as seismic-induced permeability enhancement or acoustic wave attenuation in partially saturated zones.

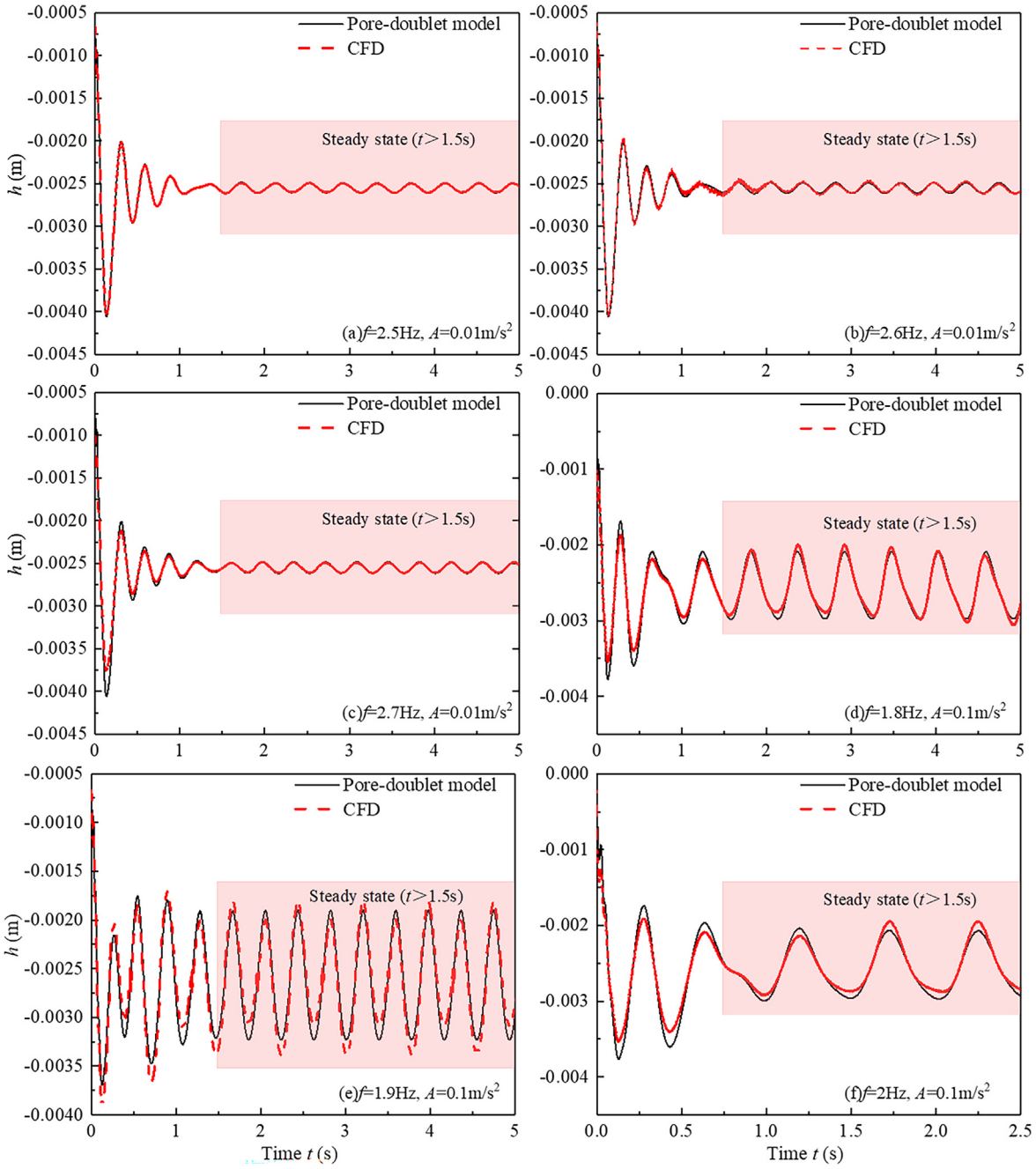

FIG. 9. Detailed time-domain validation of the pore-doublet model around its resonance frequencies. The black solid lines represent the theoretical model predictions, and the red dashed lines represent CFD simulation results. The shaded regions ($t > 1.5$ s) indicate the steady-state phase used for amplitude comparison. (a)–(c) Linear regime ($A = 0.01$ m/s^2): Comparison at frequencies of 2.5, 2.6 (resonance), and 2.7 Hz. The excellent agreement confirms the accuracy of the model in the linear range. (d)–(f) Nonlinear regime ($A = 0.1$ m/s^2): Comparison at frequencies of 1.8, 1.9 (resonance), and 2.0 Hz. The CFD results verify the downward frequency shift (softening) predicted by the theory.

B. Frequency dependence of bypass flow effects

The influence of bypass flow on bubble oscillation is strongly dependent on excitation frequency, and this frequency dependence reflects underlying differences in pressure redistribution and fluid inertia within the system. At low excitation frequencies, the fluid has sufficient time to adjust, resulting in relatively uniform pressure across the bypass channel and weak coupling to the main flow path. However, as the frequency increases, the timescale of oscillation

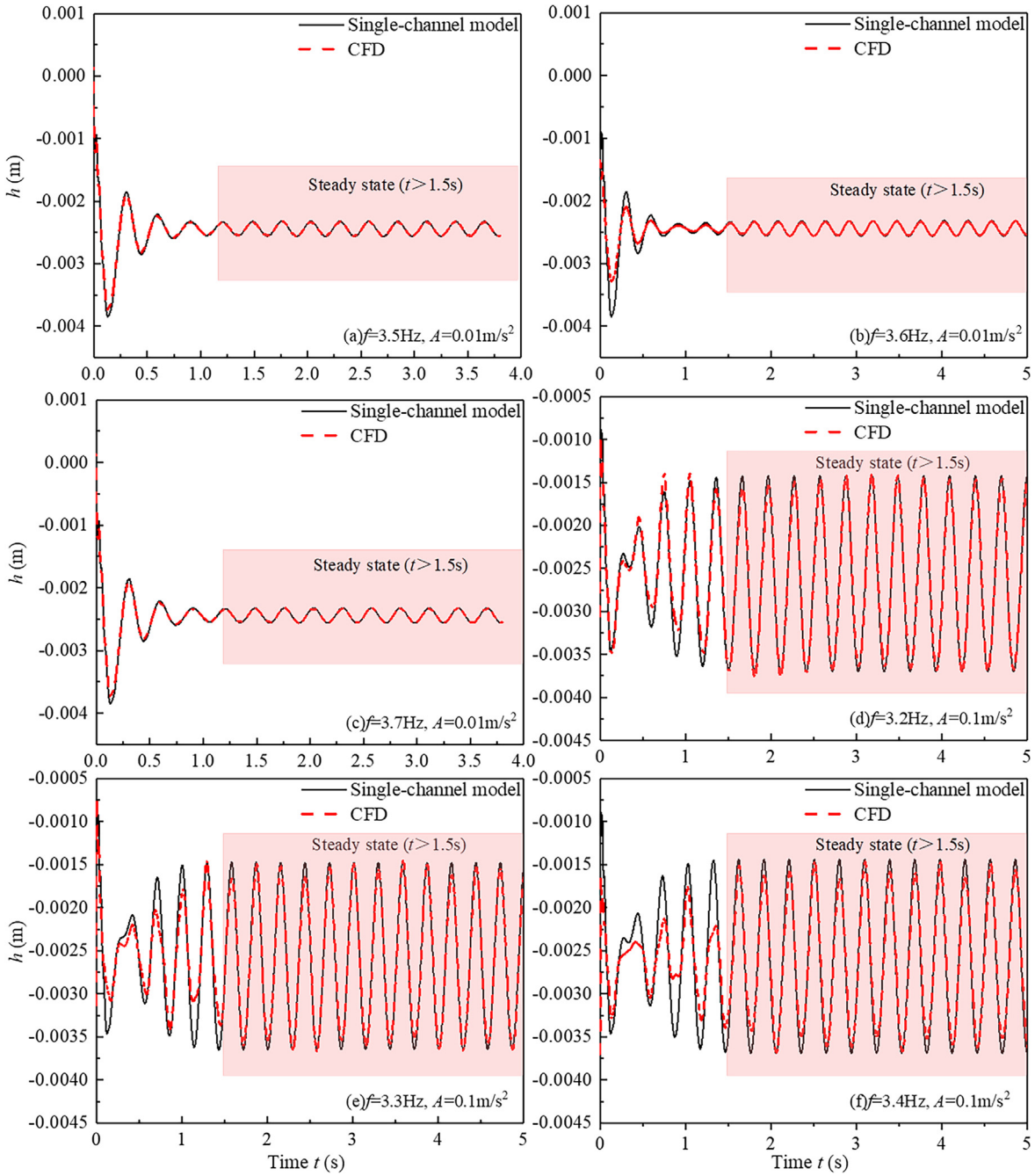

FIG. 10. Detailed time-domain validation of the single-channel model around its resonance frequencies. The subplots display the displacement response h(t) under different excitation conditions. (a)–(c) Linear regime ($A = 0.01$ m/s^2): Validation at 3.5, 3.6 (resonance), and 3.7 Hz. The theoretical and numerical curves are nearly identical, demonstrating high predictive fidelity. (d)–(f) Nonlinear regime ($A = 0.1$ m/s^2): Validation at 3.2, 3.3, and 3.4 Hz (resonance). Despite the larger amplitudes, the model effectively captures the dynamic response and the slight resonance shift.

approaches or exceeds the hydraulic response time of the bypass conduit. This mismatch leads to transient pressure differentials and inertial lags that significantly enhance the interaction between the bypass and primary channels.

Such behavior has been reported in multiphase microfluidics and acoustic streaming systems, and its implications for bubble dynamics in porous media remain underexplored.[52–54] Accordingly, within the frequency range considered in this study (0.1–10 Hz), the dynamic

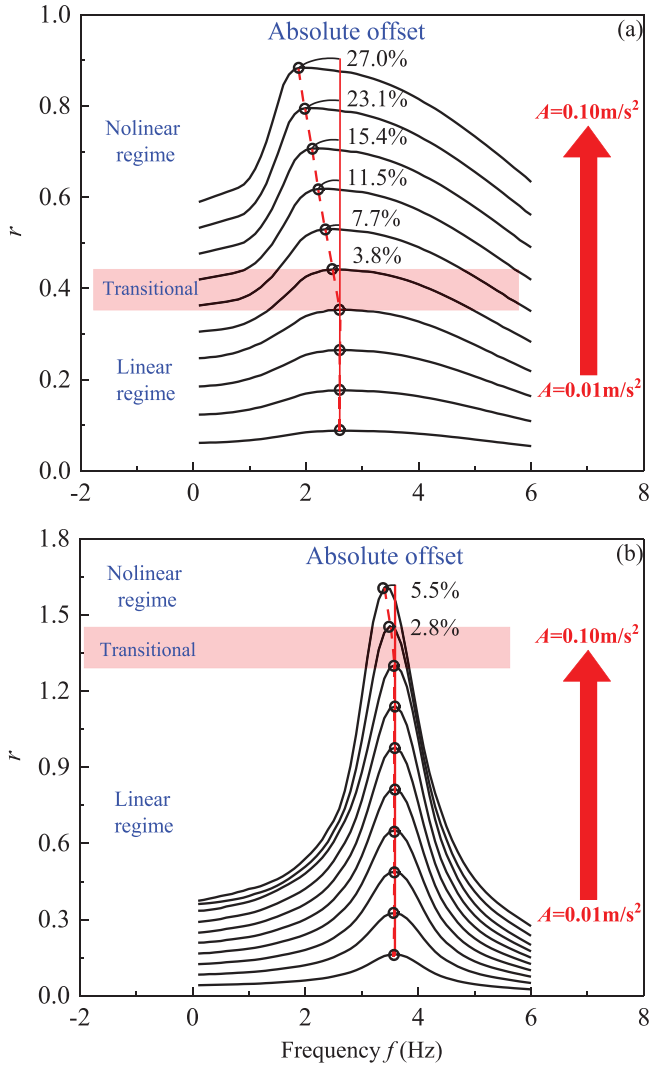

FIG. 11. Variation of the frequency response function with increasing amplitude. The left panel illustrates three distinct stages as the amplitude increases, including the linear, transition, and nonlinear stages. The central part of the image shows the absolute frequency shift of the resonance frequency at the current amplitude compared to the resonance frequency in the linear stage, after entering the nonlinear regime. The right panel uses arrows to indicate the shift of the frequency response curve from the bottom to the top, corresponding to increasing amplitude; (a) shows the results for the pore-doublet model; (b) shows the results for the single-channel model.

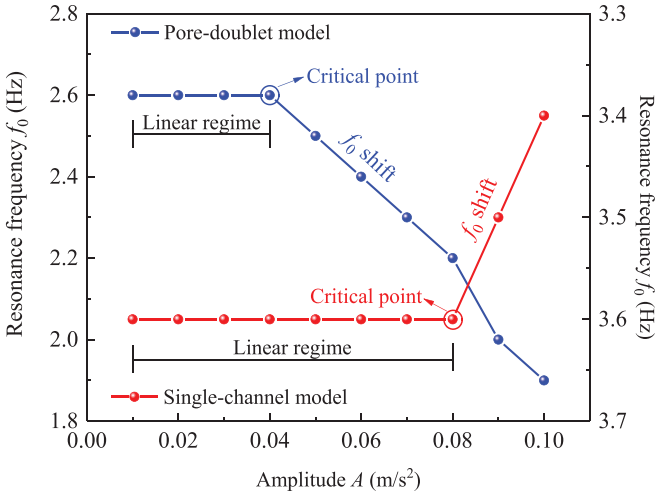

FIG. 12. Variation of resonance frequency with excitation amplitude. The figure shows the resonance frequency changes for the pore-doublet model (red line) and the single-channel model (blue line) at different excitation amplitudes. The linear regions for each model are marked with black arrows. The critical amplitudes for the transition from the linear to nonlinear stage are 0.04 m/s^2 for the pore-doublet model and 0.08 m/s^2 for the single-channel model.

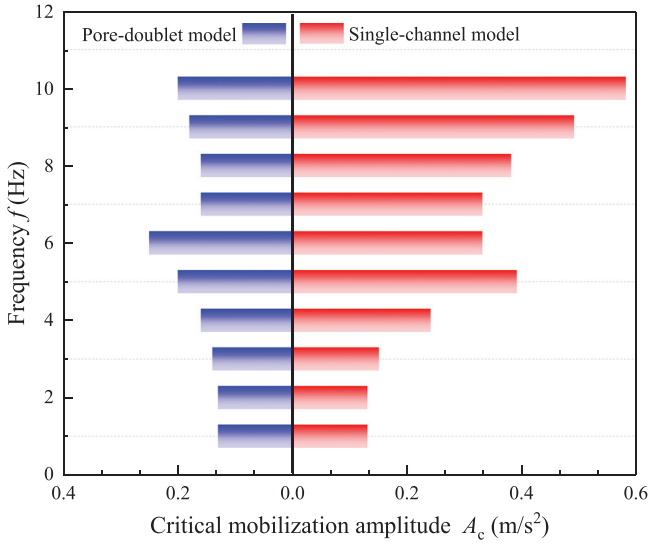

FIG. 13. Comparison of the critical mobilization amplitude as a function of frequency for the single-channel model and the pore-doublet model. The red bars represent the single-channel model, and the blue bars represent the pore-doublet model. The fluid properties are $\sigma = 0.045$ N/m, $\rho_w = 1000$ kg/m^3 $\mu_w = 0.001$ Pa s.

influence of bypass flow becomes progressively more pronounced with increasing excitation frequency, and is particularly significant at the higher end of the frequency spectrum.

It is important to emphasize that the theoretical model developed in this work does not impose a fixed frequency threshold for the onset of bypass effects. Instead, the role of bypass flow emerges naturally through the unsteady solutions of the coupled governing equations across varying frequencies. In particular, the construction of the frequency response function explicitly incorporates the dynamic coupling between the bypass channel and the primary flow path at the mathematical level, ensuring continuity and physical consistency of the model across the full range of excitation frequencies.

C. Model limitations

The current modeling framework incorporates several simplifying assumptions that, while enhancing analytical tractability and

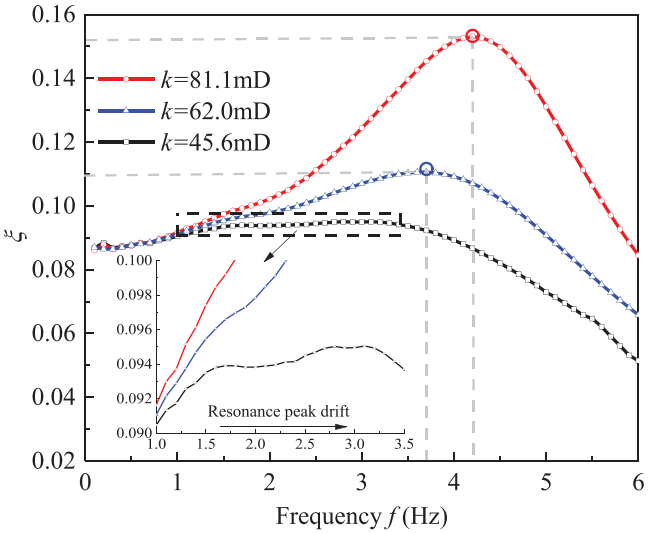

FIG. 14. Change of ξ with respect to the excited frequency f under the effect of permeability. The permeabilities of the straight tubes are 45.6, 62.0, and 81.1 mD, respectively. The resonance frequencies are 3.1, 3.6, and 4.2 Hz, respectively.

physical clarity, also impose limitations in representing the complexity of real-world subsurface environments: (i) excitation conditions are idealized as purely harmonic with simplified hydraulic boundary conditions. In contrast, real-world excitation is often broadband, intermittent, and path-dependent, potentially activating additional mechanisms such as acoustic radiation damping that are not accounted for in this model.; (ii) fluid composition and interfacial processes are simplified by assuming a thermochemically inert, immiscible two-phase system. As a result, interfacial phenomena such as rupture, coalescence, gas dissolution, and phase change, which may be triggered under high-intensity or long-duration excitation, are excluded;[55,56] (iii) material properties, including viscosity, density, and compressibility, are treated as spatially and temporally constant. However, *in situ* thermal and compositional gradients in geological formations can induce spatial variability in fluid rheology and compressibility;[57,58] (iv) bubble interactions are neglected by focusing on the dynamics of a single trapped bubble. In natural settings, interactions between multiple bubbles or droplets, such as pressure field shadowing, superposition, and collective resonance modes, can substantially alter mobilization thresholds and frequency response spectra; (v) pore geometry is represented by a periodic, smooth-walled pore-doublet structure with a single characteristic length scale. This simplification omits critical heterogeneities such as pore-size distribution, connectivity disorder, and surface roughness, which may lead to capillary pinning, localized stress concentrations, and transient fluid-solid coupling across adjacent pores.[59,60] (vi) Gravity and buoyancy effects are neglected by assuming an axisymmetric alignment. To rigorously assess the validity of this simplification, we calculate the Bond number ($Bo = \Delta\rho g r^2/\sigma$) using representative parameters ($\Delta\rho = 1000\,\mathrm{kg/m^3}$, $r = 0.5\,\mathrm{mm}$, $\sigma = 0.045\,\mathrm{N/m}$). The resulting $Bo \approx 0.05 \ll 1$ confirms that capillary forces significantly outweigh gravitational forces in defining the bubble shape. However, in horizontal arrangements, even weak buoyancy can induce transverse bubble migration, leading to asymmetric wetting films (thinning at the top wall). This asymmetry typically enhances viscous dissipation compared to the concentric assumption employed here. Therefore, while neglecting gravity is justified for isolating the bypass-induced inertial and capillary mechanisms, it represents an idealized condition that may underestimate the total system damping compared to physical experiments where film drainage plays a role.

Collectively, these assumptions constrain the quantitative applicability of the model to near-idealized conditions. Without case-specific calibration or experimental validation, predicted resonance amplitudes and mobilization thresholds should be interpreted as upper-bound estimates, rather than precise forecasts for complex natural systems.

VI. CONCLUSION

This study develops a pore-scale theoretical and computational framework that explicitly incorporates bypass flow to investigate the nonlinear oscillatory behavior and mobilization of trapped gas bubbles in porous media under vibrational forcing. By extending the classical single-channel model to a pore-doublet geometry, the analysis demonstrates that the presence of a bypass pathway significantly modifies the dynamic balance between capillary, inertial, and viscous forces. Analytical derivations and numerical simulations show that the added oscillating mass and viscous dissipation introduced by bypass flow lower the natural resonance frequency, broaden the damping response, and suppress resonance amplification. These critical dynamics are consistently underestimated in conventional single-channel models.

The proposed pore-doublet model captures both linear and nonlinear regimes of bubble dynamics across a range of excitation amplitudes and frequencies. Time-domain simulations reveal that the pore-doublet model predicts lower mobilization thresholds than the single-channel model, particularly under resonant conditions, due to enhanced pressure redistribution and increased shear-induced energy dissipation. The model also quantifies how variations in the permeability of adjacent pores modulate oscillation frequency and amplitude, thereby providing a predictive tool to relate vibrational response to microscale structural features of the pore network.

This work highlights bypass flow as a critical and previously underexplored mechanism governing bubble resonance, damping, and mobilization in vibrated porous systems. By integrating theoretical modeling with CFD validation, the proposed framework offers new physical insights and establishes a broadly applicable modeling strategy for analyzing two-phase dynamics under oscillatory forcing. The findings are relevant to a range of engineering and geophysical applications, including enhanced oil recovery, carbon dioxide sequestration, subsurface remediation, and microfluidic system design.

SUPPLEMENTARY MATERIAL

See the supplementary material for data used in this study are available at Zenodo (DOI:10.5281/zenodo.18165681) and can be accessed at the following link: https://zenodo.org/records/18165681 (Supporting_Information_Data_File).

ACKNOWLEDGMENTS

This work was supported by the National Natural Science Foundation of China (Grant No. 42277157). We would like to express our sincere gratitude to the editor and the four anonymous reviewers for their time and effort. Their insightful and constructive comments have significantly improved the quality and clarity of this manuscript.

AUTHOR DECLARATIONS

Conflict of Interest

The authors have no conflicts to disclose.

Author Contributions

Wen Deng: Conceptualization (equal); Data curation (equal); Formal analysis (equal); Funding acquisition (equal); Methodology (equal); Software (equal); Supervision (equal); Validation (equal); Visualization (equal); Writing – original draft (equal); Writing – review & editing (equal). **Shilin Yu:** Conceptualization (equal); Data curation (equal); Formal analysis (equal); Funding acquisition (equal); Methodology (equal); Software (equal); Supervision (equal); Validation (equal); Visualization (equal); Writing – original draft (equal); Writing – review & editing (equal). **Wenbao Zheng:** Software (equal); Validation (equal); Visualization (equal); Writing – original draft (equal); Writing – review & editing (equal). **Chao Zeng:** Methodology (equal); Supervision (equal); Validation (equal); Visualization (equal); Writing – review & editing (equal). **Chao-Zhong Qin:** Formal analysis (equal); Methodology (equal); Supervision (equal); Visualization (equal); Writing – review & editing (equal).

DATA AVAILABILITY

The data that support the findings of this study are available within the article and its supplementary material.

APPENDIX A: CONTROL-VOLUME DERIVATION OF THE GOVERNING EQUATION

The average velocity $\langle v_x \rangle$ of the downstream meniscus can be expressed as

$$\langle v_x \rangle = \frac{\lambda^2(h)}{\lambda^2(x)} \frac{dh}{dt}. \tag{A1}$$

The viscous force along the wall surface in control volume is

$$F_x = -8\pi\mu\lambda^2(h) N1(h) \frac{dh}{dt}, \tag{A2}$$

where we define $N1(x)$ as

$$N1(x) = \int_h^x \frac{1}{\lambda^2(\psi)} d\psi. \tag{A3}$$

The momentum efflux is

$$\rho A_d \langle v_x \rangle^2 = \frac{4}{3}\pi\rho \frac{\lambda^4(h)}{\lambda^2(x)} \left(\frac{dh}{dt}\right)^2. \tag{A4}$$

The rate of momentum change becomes

$$\rho \frac{d}{dt} \int_V \langle v_x \rangle dV = \pi\rho\lambda^2(h) \left[(L_d - h) \frac{d^2h}{dt^2} - \left(\frac{dh}{dt}\right)^2 \right]. \tag{A5}$$

The pressure along the capillary in domain II integrates from $x = h$ to x

$$P(x) = P_{II} - 8\mu_w \lambda^2(s) N2(x) - \rho a(t)(x - h), \tag{A6}$$

where we define $N2(x)$ as

$$N2(x) = \int_h^x \frac{1}{\lambda^4(\psi)} d\psi. \tag{A7}$$

The pressure force along the constricted wall is

$$F_p = 2\pi \int_h^{L_d} P(x)\lambda(x) d\lambda(x). \tag{A8}$$

Substituting Eq. (A6) into Eq. (A8) gives

$$\begin{aligned} F_p = {} & \pi P_{II} \left[\lambda^2(L_d) - \lambda^2(h)\right] - 16\mu\lambda^2(h) N3(h) \frac{dh}{dt} \\ & - \pi\lambda^2(h)\rho a(t)(L_d - h) + \pi\rho a(t) N4(h), \end{aligned} \tag{A9}$$

where we define $N3(x)$ and $N4(x)$ as

$$N3(x) = \int_h^x N2(x)\lambda(x) d\lambda(x), \tag{A10}$$

$$N4(x) = \int_h^x \lambda^2(\psi) d\psi. \tag{A11}$$

The hydraulic pressure in domain I near the upstream meniscus P_{II} is related to the gas pressure in a bubble by the Young–Laplace equation as

$$P_{II} = P_g - \frac{2\sigma}{\lambda_{men}(h)}, \tag{A12}$$

where $\lambda_{men}(h_0)$ is the radius of curvature of the meniscus at $x = h_0$.

At the initial stationary state ($t = 0$), the fluid in domain I is assumed to be static, and the Young–Laplace equation can relate the entrance pressure to the gas pressure by

$$P_g^i = P_d^i + \frac{2\sigma}{\lambda_{men}(h)}. \tag{A13}$$

Substitution of Eq. (23) into Eq. (A13) gives the transient pressure P_{II} as

$$P_{II} = \frac{P_g^i V_g^i}{V_g} - \frac{2\sigma}{\lambda_{men}(h)}. \tag{A14}$$

The exit pressure force in the control volume is

$$P_{II} A_{II} = \pi\lambda^2(h) P_{II}. \tag{A15}$$

The entrance pressure force is

$$P_d A_d = \pi\lambda^2(L_d) P_d. \tag{A16}$$

Substituting Eqs. (22), (A2), (A4), (A9), (A15), and (A16) into Eq. (31) produces the governing equation in control volume II

$$\begin{aligned} \rho\lambda^2(h)(L_d - h)\frac{d^2h}{dt^2} = {} & \rho\lambda^2(h)\left(\frac{dh}{dt}\right)^2 - \frac{4}{3}\rho\frac{\lambda^4(h)}{\lambda^2(x)}\left(\frac{ds}{dt}\right)^2 \\ & + \Delta P\lambda^2(L_d) - 16\mu\lambda^2(h) N3(h)\frac{dh}{dt} \\ & - 8\mu\lambda^2(h) N1(h)\frac{dh}{dt} - \rho\lambda^2(h) a(t)(L_d - h), \end{aligned} \tag{A17}$$

where

$$\Delta P = \frac{P_g^i V_g^i}{V_g} + \frac{2\sigma}{\lambda_{men}(h)} - P_d, \tag{A18}$$

when $P_u - P_d$ is a fixed value, Eqs. (29) and (A17) represent the single-channel model of the bubble.

APPENDIX B: DERIVATION OF THE LINEAR FREQUENCY RESPONSE FUNCTION

The bubble is subjected to external vibration excitation. Equation (8) can be expressed in a complex form

$$a(t) = a(\omega)e^{-i\omega t}. \tag{B1}$$

In this paper, we will analyze whether the downstream meniscus of the bubble exhibits overshoot phenomena. Therefore, we will construct a frequency response function based on the bubble's downstream meniscus. The transient positions of h can be expressed as

$$h(t) = h_0 + \Delta h e^{-i\omega t}, \tag{B2}$$

where h_0 is the initial position of the downstream meniscus of the bubble at the contact point, the rigorous expression for the small displacement is: $\Delta h/h_0 \ll 1$

In addition, based on Eq. (B2), the velocity and acceleration can be formulated as

$$\frac{dh}{dt} = -i\omega\Delta h e^{-i\omega t}, \tag{B3}$$

$$\frac{d^2h}{dt^2} = -\omega^2\Delta h \cdot e^{-i\omega t}. \tag{B4}$$

For the sole purpose of deriving a linearized analytical solution for small-amplitude microseisms, we introduce a simplifying assumption that the volume change is negligible relative to the initial volume ($\Delta V \ll V_0$). It is important to note that this linearization is not applied in the full nonlinear time-domain simulations presented in Sec. IV, where the exact thermodynamic pressure-volume relationship [Eq. (23)] is rigorously solved, and we can obtain

$$\Delta P = P_g^i - \frac{2\sigma}{\lambda_{men}(h+\Delta h)} - P_d. \tag{B5}$$

Substituting Eq. (A13) into Eq. (B5), we can obtain

$$\Delta P = \frac{2\sigma}{\lambda_{men}(h_0)} - \frac{2\sigma}{\lambda_{men}(h_0+\Delta h)}. \tag{B6}$$

Apply the linear approximation to Eq. (B6) to linearize the relationship between pressure difference and displacement

$$\Delta P = -2\sigma\frac{f(\beta,\Lambda,x^*)}{r_{min}^2}\Delta h. \tag{B7}$$

While in the pore-doublet model, it is expressed as

$$\Delta P = -2\sigma\frac{f(\beta,\Lambda,x^*)}{r_{min}^2}\Delta h + \frac{8\mu_w L\lambda^2(h)}{r^4} i\omega\Delta h - \rho_w a(\omega)L, \tag{B8}$$

where

$$f(\beta,\Lambda,x^*) = \frac{\pi^2}{2\beta\Lambda}\frac{-\xi^-\sin(\pi x^*)}{\left[\xi^+ - \xi^-\cos(\pi x^*)\right]^2}\frac{2 - 2\left[\frac{\Lambda}{\beta}\xi^-\cos(\pi x^*)\right]^2 + \left(\frac{\Lambda}{\beta}\right)^2\xi^+\xi^-\cos(\pi x^*)}{\left[1 + \left(\frac{\Lambda}{\beta}\xi^-\sin(\pi x^*)\right)^2\right]^{3/2}}. \tag{B9}$$

By substituting Eqs. (B1)–(B9) into Eq. (32) we can obtain

$$-\rho_w\lambda^2(h)(L_d-h)\omega^2\Delta h = -2\sigma\frac{f(\beta,\Lambda,x^*)}{r_{min}^2}\lambda^2(L_d)\Delta h + 16\lambda^2(h)\mu_w M3(s)i\omega\Delta h + 8\lambda^2(h)\mu_w M1(s)i\omega\Delta h - \rho_w\lambda^2(h)a(\omega)(L_d-h), \tag{B10a}$$

$$\begin{aligned}-\rho_w\lambda^2(h)(L_d-h)\omega^2\Delta h = &-2\sigma\frac{f(\beta,\Lambda,x^*)}{r_{min}^2}\lambda^2(L_d)\Delta h + \frac{8\mu_w L\lambda^2(L_d)}{r^4} i\omega\Delta h - \rho_w\lambda^2(L_d)a(\omega)L)\\ &+ 16\lambda^2(h)\mu_w M3(s)i\omega\Delta h + 8\lambda^2(h)\mu_w M1(s)i\omega\Delta h - \rho_w\lambda^2(h)a(\omega)(L_d-h).\end{aligned} \tag{B10b}$$

In Eqs. (B10a) and (B10b), the second term in the right-hand side has a second-order of Δh, which can be neglected in this study.

Equations (B11a) and (B11b) can be rearranged

$$\chi^I(\omega) = \frac{\rho_w(L_d-h)\lambda^2(h)}{2\sigma\frac{f(\beta,\Lambda,x^*)\lambda^2(L_d)}{r_{min}^2(\omega_c^w)^2} - \left[\left(\frac{\omega}{\omega_c^w}\right)^2\lambda^2(h)\left(\rho_w(L_d-h) + \left(16\mu_w M3(h) + 8\mu_w M1(h)\right)\frac{i}{\omega}\right)\right]}, \tag{B11a}$$

$$\chi^{II}(\omega) = \frac{\rho_w(L_d-h+L)\lambda^2(h)}{2\sigma\frac{f(\beta,\Lambda,x^*)\lambda^2(L_d)}{r_{min}^2(\omega_c^w)^2} - \left[\left(\frac{\omega}{\omega_c^w}\right)^2\lambda^2(h)\left(\rho_w(L_d-h) + \left(16\mu_w M3(h) + 8\mu_w M1(h) + \frac{8\mu_w L\lambda^2(h)}{{r_{11}}^4}\right)\frac{i}{\omega}\right)\right]}. \tag{B11b}$$

The Roman numerals "I," and "II" are used as the superscript to differentiate other frequency response functions, which will be used in the later part.

As an analogy to the second-order harmonic oscillator system, the natural frequency of the bubble is

$$\omega_0^I = \sqrt{2\sigma \frac{f(\beta,\Lambda,x^*)\lambda^2(L_d)}{\rho_w(L_d-h)r_{min}^2}}, \tag{B12}$$

$$\omega_0^{II} = \sqrt{2\sigma \frac{f(\beta,\Lambda,x^*)\lambda^2(L_d)}{\rho_w(L_d-h+L)r_{min}^2}}. \tag{B13}$$

The dimensionless natural frequency is

$$X_0 = \frac{\omega_0}{\omega_c^w}. \tag{B14}$$

The dimensionless excitation frequency in the wetting phase was defined as

$$X_w = \frac{\omega}{\omega_c^w}. \tag{B15}$$

By using Eqs. (B12)–(B15), Eqs. (B11a) and (B11b) can be reformulated as:

$$\chi^I(\omega) = \frac{1}{\left(X_0^I\right)^2 - \left(X_w^I\right)^2\left(\lambda^2(h)\dfrac{\rho_w(L_d-h)+(16\mu_w M3(s)+8\mu_w M1(s))\ i}{\rho_w(L_d-h)\qquad\qquad X_w^I}\right)}, \tag{B16a}$$

$$\chi^{II}(\omega) = \frac{1}{\left(X_0^{II}\right)^2 - \left(X_w^{II}\right)^2\left(\lambda^2(h)\dfrac{\rho_w(L_d-h)+\left(16\mu_w M3(s)+8\mu_w M1(s)+\frac{8\mu_w L\lambda^2(s)}{r^4}\right)\ i}{\rho_w(L_d-h+L)\qquad\qquad\qquad X_w^{II}}\right)}. \tag{B16b}$$

REFERENCES

[1]M. A. Abrams, "Significance of hydrocarbon seepage relative to petroleum generation and entrapment," Mar. Pet. Geol. **22**, 457–477 (2005).

[2]R. T. Amos, K. U. Mayer, B. A. Bekins, G. N. Delin, and R. L. Williams, "Use of dissolved and vapor-phase gases to investigate methanogenic degradation of petroleum hydrocarbon contamination in the subsurface," Water Resour. Res. **41**, W02001, https://doi.org/10.1029/2004WR003433 (2005).

[3]M. M. Krol, K. G. Mumford, R. L. Johnson, and B. E. Sleep, "Modeling discrete gas bubble formation and mobilization during subsurface heating of contaminated zones," Adv. Water Resour. **34**, 537–549 (2011).

[4]R. Enouy, M. Li, M. A. Ioannidis, and A. J. A. Unger, "Gas exsolution and flow during supersaturated water injection in porous media: II. Column experiments and continuum modeling," Adv. Water Resour. **34**, 15–25 (2011).

[5]X. Zheng and J. Jang, "Hydraulic properties of porous media saturated with nanoparticle-stabilized air–water foam," Sustainability **8**, 1317 (2016).

[6]R. Bora, B. B. Maini, and A. Chakma, "Flow visualization studies of solution gas drive process in heavy oil reservoirs with a glass micromodel," SPE Reserv. Eval. Eng. **3**, 224–229 (2000).

[7]J. Jang and J. C. Santamarina, "Recoverable gas from hydrate-bearing sediments: Pore network model simulation and macroscale analyses," J. Geophys. Res. **116**, B08202, https://doi.org/10.1029/2010JB007841 (2011).

[8]X. Zheng, N. Mahabadi, T. S. Yun, and J. Jang, "Effect of capillary and viscous force on CO_2 saturation and invasion pattern in the microfluidic chip," JGR Solid Earth **122**, 1634–1647 (2017).

[9]J. J. Taber, "Dynamic and static forces required to remove a discontinuous oil phase from porous media containing both oil and water," Soc. Pet. Eng. J. **9**, 3–12 (1969).

[10]J. C. Melrose and C. F. Brandner, "Role of capillary forces in determining microscopic displacement efficiency for oil recovery by waterflooding," J. Can. Pet. Technol. **13**, 54–62 (1974).

[11]M. Manga, I. Beresnev, E. E. Brodsky, J. E. Elkhoury, D. Elsworth, S. E. Ingebritsen, D. C. Mays, and C.-Y. Wang, "Changes in permeability caused by transient stresses: Field observations, experiments, and mechanisms," Rev. Geophys. **50**, RG2004, https://doi.org/10.1029/2011RG000382 (2012).

[12]W. Deng, I. Beresnev, and M. Cardenas, "Dynamics of trapped nonwetting phase droplet under seismic stimulation in constricted pores," in *AGU Fall Meeting Abstracts* (AGU, 2012), p. H51N-03.

[13]N. Tisato, B. Quintal, S. Chapman, Y. Podladchikov, and J.-P. Burg, "Bubbles attenuate elastic waves at seismic frequencies: First experimental evidence," Geophys. Res. Lett. **42**, 3880–3887, https://doi.org/10.1002/2015GL063538 (2015).

[14]M. L. Rudolph and M. Manga, "Frequency dependence of mud volcano response to earthquakes," Geophys. Res. Lett. **39**, L14303, https://doi.org/10.1029/2012GL052383 (2012).

[15]D. Krapf, B. M. Quinn, M.-Y. Wu, H. W. Zandbergen, C. Dekker, and S. G. Lemay, "Experimental observation of nonlinear ionic transport at the nanometer scale," Nano Lett. **6**, 2531–2535 (2006).

[16]A. Sojahrood, H. Haghi, R. Karshafian, and M. Kolios, "Critical corrections to formulations of nonlinear energy dissipation of ultrasonically excited bubbles and a unifying parameter to assess and enhance bubble activity in applications," arXiv:1909.04864 (2019).

[17]A. J. Sojahrood and M. C. Kolios, "Nonlinear oscillations and resonances of the acoustic bubble and the mechanisms of energy dissipation," in *Energy Aspects of Acoustic Cavitation and Sonochemistry* (Elsevier, 2022), pp. 109–131.

[18]I. A. Beresnev, "Theory of vibratory mobilization on nonwetting fluids entrapped in pore constrictions," Geophysics **71**, N47–N56 (2006).

[19]M. Hilpert, "Capillarity-induced resonance of blobs in porous media: Analytical solutions, lattice-Boltzmann modeling, and blob mobilization," J. Colloid Interface Sci. **309**, 493–504 (2007).

[20]M. Hilpert, G. H. Jirka, and E. J. Plate, "Capillarity-induced resonance of oil blobs in capillary tubes and porous media," Geophysics **65**, 874–883 (2000).

[21]W. Deng and M. B. Cardenas, "Dynamics and dislodgment from pore constrictions of a trapped nonwetting droplet stimulated by seismic waves," Water Resour. Res. **49**, 4206–4218, https://doi.org/10.1002/wrcr.20335 (2013).

[22]T. M. Al-Shami, S. R. Jufar, G. N. Hamada, D. A. Kanesan, and U. Djuraev, "Effect of seismic excitation on mobilization of trapped oil globule in pore doublet model," Int. J. Mech. Eng. Robot. Res. **8**, 998–1002 (2019).

[23]S.-Y. Hsu, J. Katz, and M. Hilpert, "Theoretical and experimental study of resonance of blobs in porous media," Geophysics **77**, EN61–EN71 (2012).

[24]Z. Li, Y. Li, Y. Su, and W. Tian, "The shale gas flow in the complex porous media based on the lattice Boltzmann method," Phys. Fluids **36**, 122019 (2024).

[25]I. Rasuceanu and C. Patrascu, "Capillary flow of two immiscible liquids initially separated by a Taylor gas bubble," Phys. Fluids **36**, 012110 (2024).
[26]I. Chatzis and F. Dullien, "Dynamic immiscible displacement mechanisms in pore doublets: Theory versus experiment," J. Colloid Interface Sci. **91**, 199–222 (1983).
[27]T. S. Lundström, L. H. Gustavsson, N. Jēkabsons, and A. Jakovics, "Wetting dynamics in multiscale porous media: Pore-doublet model, experiment, and theory," AIChE J. **54**, 372–380 (2008).
[28]F. S. Magnani, P. C. Philippi, Z. R. Liang, and C. P. Fernandes, "Modelling two-phase equilibrium in three-dimensional porous microstructures," Int. J. Multiphase Flow **26**, 99–123 (2000).
[29]Y. Wu, P. Tahmasebi, C. Lin, L. Ren, and Y. Zhang, "Quantitative characterization of non-wetting phase in water-wet porous media based on multiphase flow experiment and numerical simulation," J. Pet. Sci. Eng. **188**, 106914 (2020).
[30]Y. Han, G. Mutschke, and K. Eckert, "A geometric interpolation scheme for applying dynamic wetting to three-dimensional volume of fluid simulations," arXiv:2509.21076 (2025).
[31]A. Pistiner, M. Shapiro, and H. Rubin, "Gravitational migration of fuel in porous media," Transp. Porous Media **9**, 187–205 (1992).
[32]Y. Ma, Y. Cheng, Y. Shen, J. Xu, and Y. Sui, "Manipulation of bubble migration through thermal capillary effect under variable buoyancy," Int. J. Therm. Sci. **149**, 106199 (2020).
[33]J. Rivero-Rodriguez and B. Scheid, "Bubble dynamics in microchannels: Inertial and capillary migration forces," J. Fluid Mech. **842**, 215–247 (2018).
[34]Z. Zhang, R. Wu, and C. Zhao, "Pore-scale study of buoyancy-driven gas bubble migration, breakup, trapping, and coalescence in the near injection region of liquid-saturated porous media," Ind. Eng. Chem. Res. **60**, 12419–12428 (2021).
[35]Z. Wang, J. Zhang, X. Liu, H. Zhao, D. Ren, Y. Qi, Y. Yuan, and Q. Kang, "Influence of aspect ratio of migration space on gas migration and accumulation mechanisms of different types of gas reservoirs," Nat. Resour. Res. **34**, 427–457 (2025).
[36]P. A. Gauglitz and C. J. Radke, "Dynamics of Haines jumps for compressible bubbles in constricted capillaries," AIChE J. **35**, 230–240 (1989).
[37]C. Zeng and W. Deng, "Effect of subsurface microseisms on the motion of dispersed droplets in pores," J. Geophys. Res. Solid Earth **125**, e2019JB018783, https://doi.org/10.1029/2019JB018783 (2020).
[38]C. E. Brennen, *Cavitation and Bubble Dynamics* (Oxford University Press, Oxford, 1995).
[39]A. Carrella and D. J. Ewins, "Identifying and quantifying structural nonlinearities in engineering applications from measured frequency response functions," Mech. Syst. Signal Process. **25**, 1011–1027 (2011).
[40]D. E. Adams, "Frequency domain ARX model and multi-harmonic FRF estimators for non-linear dynamic systems," J. Sound Vib. **250**, 935–950 (2002).
[41]A. Prosperetti, L. A. Crum, and K. W. Commande, "Nonlinear bubble dynamics," J. Acoust. Soc. Am. **83**, 502–514 (1988).
[42]C. Zeng, W. Deng, and M. B. Cardenas, "Resonance of droplets in constricted capillary tubes: Critical factors and nonlinearity," Phys. Rev. Fluids **5**, 08360 (2020).
[43]T. C. Sykes, A. A. Castrejón-Pita, J. R. Castrejón-Pita, D. Harbottle, Z. Khatir, H. M. Thompson, and M. C. T. Wilson, "Surface jets and internal mixing during the coalescence of impacting and sessile droplets," Phys. Rev. Fluids **5**, 023602 (2020).
[44]S.-I. Yeh, W.-F. Fang, H.-J. Sheen, and J.-T. Yang, "Droplets coalescence and mixing with identical and distinct surface tension on a wettability gradient surface," Microfluid. Nanofluid. **14**, 785–795 (2013).
[45]E. V. Veitsman, "Effect of fluctuations on the surface tension of liquid droplets and gas bubbles and their nucleation," Theor. Found. Chem. Eng. **41**, 309–314 (2007).
[46]M. N. Shneider and M. Pekker, "Surface tension of small bubbles and droplets and the cavitation threshold," arXiv:1901.04329 (2019).
[47]K.-L. Pan, K.-L. Huang, W.-T. Hsieh, and C.-R. Lu, "Rotational separation after temporary coalescence in binary droplet collisions," Phys. Rev. Fluids **4**, 123602 (2019).
[48]C. Wang, Y. Lü, F. Huo, T. Ye, D. Li, and L. He, "Exploration of the dynamic attachment properties of oil droplets to air or condensate bubbles in flotation," Colloids Surf. A **703**, 135387 (2024).
[49]S. Yan, Y. Zhang, C. Peng, X. Yang, Y. Huang, Z. Bai, and X. Xu, "Oil droplet movement and micro-flow characteristics during interaction process between gas bubble and oil droplet in flotation," Chin. J. Chem. Eng. **45**, 229–237 (2022).
[50]Y. Dai, K. Yu, H. Li, H. Zhu, Q. He, T. Zhang, T. Liu, B. Luo, S. Zhang, C. Cai, Y. Wu, Y. Luo, and S. Nie, "Efficient removal of oil mist via triboelectric negative air ions," Nano Energy **126**, 109692 (2024).
[51]I. C. Christov, H. A. Stone, and F. J. Muzzio, "Hydrodynamics of bubble flow through a porous medium with applications to packed bed reactors," AIChE J. **70**, e18343 (2024).
[52]X. Shang, X. Huang, and C. Yang, "Bubble dynamics in a microfluidic chamber under low-frequency actuation," Microfluid. Nanofluid. **20**, 14 (2016).
[53]M. W. Trethewey and L. L. Koss, "Experimental evaluation of force frequency shifting for low-frequency vibration excitation," Mech. Syst. Signal Process. **18**, 535–553 (2004).
[54]A. Sengupta and P. Tucker, "Effects of forced frequency oscillations and free stream turbulence on the separation-induced transition in pressure gradient dominated flows," Phys. Fluids **32**, 104105 (2020).
[55]Y. Chen, H. Hong, and X. Shi, "Asymptotic stability of phase separation states for compressible immiscible two-phase flow with periodic boundary condition in 3D," arXiv:2105.13552 (2021).
[56]Y. Chen, Y. Peng, X. Shi, and X. Wang, "Phase transition in non-isentropic compressible immiscible two-phase flow with van der Waals equation of state," arXiv:2506.20955 (2025).
[57]A. Sharma, R. Thakur, S. Jose, and R. Govindarajan, "Viscosity variation in fluid flows across scale," arXiv:2507.23532 (2025).
[58]M. Escudier, "Fluids and fluid properties," in *Introduction to Engineering Fluid Mechanics* (Oxford University Press, Oxford, 2017), pp. 17–46.
[59]A. Jahanbakhsh, O. Shahrokhi, and M. M. Maroto-Valer, "Does structural heterogeneity overshadow the effects of wettability heterogeneity on fluid flow at pore-scale?," in Proceedings of the 16th Greenhouse Gas Control Technologies Conference (2022).
[60]S. Fagbemi, P. Tahmasebi, and M. Piri, "Interaction between fluid and porous media with complex geometries: A direct pore-scale study," Water Resour. Res. **54**, 6336–6356, https://doi.org/10.1029/2017WR022242 (2018).